JGR Planets

RESEARCH ARTICLE
10.1029/2019JE006045

Implications of Reactions Between SO_2 and Basaltic Glasses for the Mineralogy of Planetary Crusts

Christian J. Renggli[1,2], Andrew B. Palm[1], Penelope L. King[1], and Paul Guagliardo[3]

[1]Research School of Earth Sciences, The Australian National University, Canberra, ACT, Australia, [2]Now at Institute for Mineralogy, University of Münster, Münster, Germany, [3]Centre for Microscopy, Characterization and Analysis, University of Western Australia, Perth, Western Australia, Australia

Key Points:
- Basalt glass reacts with SO_2 gas to form coatings with Ca-, Mg-, Na-sulfates, Fe-, Fe-Ti-, and Ti-oxides and silica
- These reactions may be recorded and detected on Earth, Mars, Venus, and Io

Supporting Information:
- Supporting Information S1

Correspondence to:
C. J. Renggli,
renggli@uni-muenster.de

Citation:
Renggli, C. J., Palm, A. B., King, P. L., & Guagliardo, P. (2019). Implications of reactions between SO_2 and basaltic glasses for the mineralogy of planetary crusts. *Journal of Geophysical Research: Planets*, *124*, 2563–2582. https://doi.org/10.1029/2019JE006045

Received 16 MAY 2019
Accepted 27 AUG 2019
Accepted article online 3 SEP 2019
Published online 17 OCT 2019

Abstract Basalts are ubiquitous in volcanic systems on several planetary bodies, including the Earth, Mars, Venus, and Jupiter's moon Io, and are commonly associated with sulfur dioxide (SO_2) degassing. We present the results of an experimental study of reactions between SO_2 and basaltic glasses. We examined Fe-free basalt, and Fe-bearing tholeiitic and alkali basalts with a range of Fe^{3+}/Fe_{total} (0.05 to 0.79) that encompass the oxygen fugacities proposed for most terrestrial planetary bodies. Tholeiitic and alkali basalts were exposed to SO_2 at 600, 700, and 800 °C for 1 hr and 24 hr. Surface coatings formed on the reacted basalts; these contain $CaSO_4$, $MgSO_4$, Na_2SO_4, $Na_2Ca(SO_4)_2$, Fe_2O_3, Fe_3O_4, Fe-Ti-(Al)-oxides, and TiO_2. Additionally, the SO_2-basalt reaction drives nucleation of crystalline phases in the substrate to form pyroxenes and possible Fe-oxides. A silica-rich layer forms between the substrate and sulfate coatings. More oxidized basalts may readily react with SO_2 to form coatings dominated by large Ca-sulfate and oxide grains. On less oxidized basalts (NNO−1.5 to NNO−5), reactions with SO_2 will form thin, fine-grained aggregates of sulfates; such materials are less readily detected by spectroscopy and spectrometry techniques. In contrast, in very reduced basalts (lower than NNO−5), typical of the Moon and Mercury, SO_2 is typically a negligible component in the magmatic gas, and sulfides are more likely.

Plain Language Summary The primary sulfur-bearing gas species in volcanic gas is sulfur dioxide (SO_2), a very reactive gas species which may modify the chemical and mineralogical properties of magmatic rocks made of minerals and glasses. Here we investigate the reaction between sulfur dioxide and basalt glasses by conducting experiments at high temperatures (600–800 °C). The glass surfaces are altered to form sulfate and oxide coatings. This reaction likely occurred on Venus and Mars and may occur on Jupiter's moon Io. Observations of the surfaces of these planetary bodies may reveal sulfates, oxides, and silica-rich coatings on the surfaces of volcanic rocks which formed via the investigated gas-solid reaction.

1. Introduction

Basalt is the most common volcanic rock on the terrestrial planets and is typically associated with gaseous sulfur dioxide (SO_2; Basaltic Volcanism Study Project, 1981; Taylor & McLennan, 2009). On Earth, basalt makes up over half of the volcanic crust, including most of the volcanoes on the seafloor, and significant quantities of SO_2 are derived from both explosive and effusive basaltic volcanoes (Carn et al., 2016). On Mars, basaltic volcanism provided the primary source of S to the surface through both SO_2 emissions, sulfides, and sulfates; these materials were redistributed as abundant sulfate minerals on the surface (Franz et al., 2018; Gaillard & Scaillet, 2009; King & McLennan, 2010; McSween et al., 2006). On Venus, basalts are the dominant volcanic rock type (McSween et al., 2006; Nimmo & McKenzie, 1998). Thermodynamic and experimental data suggest that SO_2 interacted with the surface of basalt deposits on Venus in the past (Berger et al., 2019; Fegley & Prinn, 1989; Zolotov, 2018). Basalt dominates the surface of Io, moon of Jupiter (Blaney et al., 1995; Carr, 1986), and the magmas are sufficiently oxidizing to produce SO_2 which has been directly measured in the atmosphere and eruptive plumes (Doute, 2002; Glaze, 1999; Kumar, 1985; Pearl et al., 1979; Vandaele et al., 2017). On the Moon, basalt is also a dominant rock type (Haskin & Warren, 1991); however, SO_2 is likely negligible because oxygen fugacity (fO_2) of the volcanic gas and the magmatic source were too low (Renggli et al., 2017). Finally, Mercury has vast flood basalts (Denevi et al., 2013) and basaltic pyroclastic deposits (Kerber et al., 2011), and surface sulfur concentrations of up to 4 wt. % (Nittler et al., 2011; Starr et al., 2012; Weider et al., 2012).

Sulfur dioxide degassing from explosive and effusive eruptions provides the opportunity for SO_2 reactions with glassy particles to scavenge SO_2 and form sulfates (e.g., Ayris et al., 2013; Barone et al., 2016; Delmelle et al., 2018; Rose, 1977). On Earth, basaltic systems may degas significant amounts of SO_2 (Carn et al., 2016) allowing reactions to occur with basaltic glasses that form rapidly on the flow surface or in small fountaining events. Basaltic fissure eruptions in the 2014–2015 Holuhraun eruption (Iceland) showed rapid formation of sulfate aerosols (Ilyinskaya et al., 2017). Although the source of the cations in the sulfate aerosols is unknown, a large proportion may be from basalt particles. Sulfates formed by reactions with SO_2 are most commonly observed in volcanic ash eruptions with anhydrite the most common phase produced (Ayris et al., 2013; Barone et al., 2016). Sulfates on volcanic ash particles from the Eyjafjallajökull (Iceland) eruption in 2010, include epsomite ($MgSO_4{\cdot}7H_2O$), melanterite ($FeSO_4$), hydrated thenardite ($Na_2SO_4{\cdot}10H_2O$), and minor arcanite (K_2SO_4; Gislason et al., 2011). Studies of Hawaiian basalts have shown that SO_2-rich gases form an acid fog environment, altering basalts to form sulfate-rich coatings including anhydrite, gypsum, jarosite, natroalunite, and anatase, on amorphous silica rims (McCanta et al., 2014; Schiffman et al., 2006).

Although sulfate products from the reactions between volcanic gas and natural volcanic glass are observed in natural samples, the experimental data to constrain the mechanism of reaction were missing until relatively recently. McCollom et al. (2013) conducted experiments reacting a wet SO_2-bearing vapor with basalt at 145 °C for up to 137 days, observing the formation of coatings containing anhydrite, Fe-rich natroalunite, traces of other sulfates, and iron oxides on a layer of amorphous silica. Ayris et al. (2013) investigated reactions between dry SO_2-rich gas and tephrite, phonolite, dacite, and rhyolite glasses at temperatures up to 800 °C. They observed coatings rich in $CaSO_4$ form on the ash particles at rapid rates (within minutes) at temperatures of 300 °C and above. They suggest that the Ca-availability in the glass drives the sulfate-forming reaction. Renggli et al. (2019) studied dry, pure SO_2 reactions with anorthite-diopside (AnDi) composition glass starting materials and found a temperature dependence of the reaction products. At 600 °C (below the glass transition temperature, T_g), $CaSO_4$ and $MgSO_4$ coatings formed on the $An_{15}Di_{85}$, $An_{36}Di_{64}$ (eutectic glass), and $An_{48}Di_{52}$ glasses. At 800 °C, only $CaSO_4$ formed on all glasses (Renggli et al., 2019). In the presence of Ca in the glass, even at concentrations as low as 5 mol. %, $CaSO_4$ is the dominant reaction product on glasses in the anorthite-diopside-albite system (Renggli et al., 2019). Ayris et al. (2013) and Renggli et al. (2019) both show that the mobility of the sulfate-forming cation (e.g., Ca^{2+}) in the glass and its diffusion to the glass surface is the rate-limiting step in the reaction of SO_2 with glass starting material. These studies show that glass composition and structure are important controls for the reaction rate and sulfate compositions.

In sum, the experimental work shows that sulfur dioxide (gas) rapidly reacts with geologic materials via surface-mediated reactions, where SO_2 disproportionates to form sulfates and reduced sulfur (gas or sulfides; Burnham, 1979; Ayris et al., 2013; Henley et al., 2015, 2017; Delmelle et al., 2018; King et al., 2018; Palm et al., 2018; Renggli & King, 2018; Zolotov, 2018; Renggli et al., 2019). The reaction follows the following form:

$$2SO_{2(g)} + MO_{\text{silicate}} \rightarrow MSO_4 + S_{\text{reduced}(g)} + \text{silicate (+oxide)} \quad (1)$$

where M refers to a cation such as an alkali or alkaline earth cation (e.g., Ca^{2+}, Mg^{2+}, Na^{+}). A complete reaction with excess SO_2 results in the consumption of all alkali or alkaline earth cations. Depending on the phase and composition of the reacted MO_{silicate}, the product silicate (+oxide) consists of SiO_2 and aluminosilicates.

The reaction between pure SO_2 and Fe-bearing basalts affects the valence state of multivalent elements, such as $Fe^{2+/3+}$, in the reaction products because the gas has an effective oxygen fugacity ($\log fO_2$/1 bar, henceforth referred to as $\log fO_2$) of $\log fO_2 = -12.1$ at 700 °C (Renggli & King, 2018; i.e., 4.2 $\log fO_2$ units above the Ni-NiO (NNO) buffer). The starting glass is efficiently oxidized in a H-free system by the inward diffusion of electron holes, which are charge compensated by the outward diffusion of divalent cations such as Ca^{2+} and Mg^{2+}, where diffusivities of these cations are the rate-limiting factors (Cook & Cooper, 2000; Cooper, 2020; Cooper et al., 1996). The oxidation process results in the concentration of CaO and MgO at the glass surface and the nucleation of Fe_2O_3 in the oxidized glass (Cook & Cooper, 2000; Cooper et al., 1996).

These studies suggest that the fO_2 of the starting materials may have an important role in producing the reaction products because the initial oxidation state of Fe (Fe^{3+}/Fe^{2+}) has a role in the formation of oxides (reaction (1)) like Fe_2O_3. This is discussed in more detail in section 4.1.

Here we investigate the effect of different fO_2 states of basalt glasses on the reaction with pure SO_2 at high temperatures (>600 °C). We show that the reaction products include a range of different sulfates, oxides, and silica coatings which form within hours. We discuss the effect of different fO_2 in S-O-bearing gases on the stabilities of reaction products based on thermodynamic calculations. Using the calculated fO_2 for Earth, Mars, Venus, Io, the Moon, and Mercury, we predict the solid reaction products on the surfaces of these planetary bodies.

2. Methods

2.1. Starting Materials

The experiments were run with a synthetic Fe-free basalt, a tholeiitic basalt, and an alkali basalt with the latter two compositions simulating common basalts on planetary bodies (Basaltic Volcanism Study Project, 1981). The Fe-bearing tholeiitic basalt glass is from the 1921 Pu'u O'o eruption at Kilauea, Hawai'i (Holloway & Burnham, 1972) and the alkali basalt is from San Carlos, Arizona (King et al., 2000). The tholeiitic and alkali basalts were prepared as part of previous experimental studies and are completely crystal-free (Dufresne et al., 2015; King et al., 2000). The glass compositions were determined using an electron microprobe and Mössbauer spectroscopy (Table 1 by Dufresne et al., 2015). Additional experiments were conducted with Fe-free basalt glass to evaluate the effect of Fe, and this material was synthesized from chemical grade oxide powders. The powders were ground and mixed before melting at 1500 °C for 10 min, quenched, reground, and remelted twice at 1500 °C. The glass starting materials were analyzed using a scanning electron microscope (SEM) to ensure that they were homogeneous and crystal free. The glass chips were polished to ¼-μm grit and washed with methanol to ensure a flat and clean surface.

The tholeiitic basalts have glass transition temperatures (T_g) between 715 and 745 °C, whereas the T_g of the alkali basalt is ~640 °C (Ryan & Sammis, 1981). Consequently, some of the experiments were conducted below T_g with glass sensuo stricto, whereas for experiments conducted above T_g these samples were strictly "supercooled melts." In the general discussion we refer to all samples as basalt glasses and use the term supercooled melts only when directly referring to specific experiments on basaltic substrates conducted above T_g.

The tholeiitic basalt was preequilibrated at 1400 °C under three different oxygen fugacities corresponding to 1.5 logfO_2 units below the Ni-NiO buffer (NNO−1.5), at NNO and at NNO+1 by Dufresne et al. (2015). The corresponding Fe^{3+}/Fe_{tot} ratios were 0.22, 0.33, and 0.79 using Mössbauer spectroscopy (Dufresne et al., 2015; Table 1). The alkali basalt was preequilibrated at ~NNO−5 and NNO resulting in Fe^{3+}/Fe_{tot} ratios calculated following Kress and Carmichael (1991) of 0.05 and 0.23 (Table 1, Dufresne et al., 2015). These fO_2-conditions (~NNO−5 to NNO+1) fall in the range of redox states of magmas on planetary bodies, from Mars (NNO−5 to NNO; Hirschmann & Withers, 2008; Gaillard & Scaillet, 2009; Gaillard et al., 2013; Castle & Herd, 2017) and the Moon (NNO−6 to NNO−4, Rutherford & Papale, 2009) to Earth (NNO−3 to NNO+5; Carmichael, 1991; Ballhaus, 1993; Oppenheimer et al., 2011) and allow us to examine the effect of oxidation state of the reactant glass on the reaction mechanism.

2.2. Experimental Conditions

Polished glass chips with diameters of ~2 mm were placed on a Pt-tray which was suspended in a vertical gas mixing furnace at 600, 700, or 800 °C for 1 hr and 24 hr and exposed to a 50-sccm (ml/min) flow of SO_2. Before and after each SO_2 experiment, the furnace was purged with Ar for approximately 2 min to allow thermal equilibration before exposure to SO_2 and to remove any atmospheric contamination and to minimize escape of SO_2 into the laboratory. The experimental run products (reacted glasses) were immediately placed in a desiccator to minimize hydration of the reaction products (Dalby et al., 2018). Three aliquots of sample were run so that enough sample was available for a wide range of analytical methods (like Palm et al., 2018). Cross sections of glasses were obtained by embedding the run products in epoxy resin and cutting the mounds. The samples were cut using a dry diamond saw. The cross sections were polished with diamond paste using ¼-μm diamond grit without any water. During the preparation of cross sections, the coating

Table 1
Compositions of the Basalt Glasses Used in the Experiments (Fe-Bearing Compositions From Dufresne et al., 2015)

	Fe-free basalt	Tholeiite, NNO−1.5	Tholeiite, NNO	Tholeiite, NNO+1	Alkali basalt IW	Alkali basalt NNO
[wt.%]			Dufresne et al., 2015			
SiO_2	59.2	51.4	51.6	50.9	45.0	45.6
TiO_2	1.3	2.7	2.1	2.7	2.5	2.6
Al_2O_3	18.3	12.1	11.6	11.9	14.4	14.4
Fe_2O_3	0.0	1.6	2.6	5.3	0.7	3.3
FeO	0.0	8.8	8.8	4.4	14.1	11.0
MnO	0.0	0.2	0.2	0.2	0.2	0.2
MgO	11.1	9.9	10.5	9.9	8.0	8.3
CaO	7.6	10.7	10.3	10.6	8.1	7.9
Na_2O	1.7	1.5	2.0	1.8	4.7	4.8
K_2O	0.0	0.4	0.4	0.5	1.1	1.2
P_2O_5	0.0	0.2	0.3	0.2	0.8	0.9
Totals	99.2	99.4	100.3	98.3	99.5	100.1
Fe^{3+}/Fe_{tot}		0.22	0.33	0.79	0.05	0.23
Fe^{3+}/Na^{+}		0.41	0.50	1.14	0.06	0.26
NBO/T	0.38	0.80	0.83	0.65	0.91	0.84

was lost from some glass surfaces. This may have allowed polishing material and possible contaminants to become embedded between the sample and the embedding epoxy resin, and as such, Al-rich contamination during polishing was considered when interpreting the analyses. The polished samples were cleaned with ethanol and compressed air.

2.3. Analytical Methods

The experimental run products were investigated using scanning electron microscopy, Raman spectroscopy, and nanoSIMS element mapping. These analytical methods revealed the chemistry and mineralogy of the different phases in the coatings on the reacted basalts and the chemical modification in the reacted substrates (Dalby et al., 2018; Mernagh et al., 2018; Palm et al., 2018).

The mineral phases in the surface coatings were identified using a Renishaw 2000 inVia Reflex Raman Spectrometer equipped with a standard confocal microscope at the Research School of Physics and Engineering at the Australian National University. A Renishaw diode-pumped solid state laser provided 532 nm laser excitation. The laser was focused with a 100X objective lens, with a resulting laser power of 3 mW on the sample and a spot size of ~1 μm. Single Raman spectra were obtained using a 1-s integration time with 10 accumulations. At these conditions the laser may sample the material to a depth of 4 μm, depending on the laser transparency of the analyzed material (Mernagh et al., 2018). The 520.7-cm^{-1} band from a pure Si standard was used to test the alignment of the spectrometer prior to the analysis of the coatings.

The coatings formed by the SO_2-glass reactions on the basalt glasses were observed with Field Emission Scanning Electron Microscopy (FESEM), using a Hitachi 4300 SE/N Schottky Field Emission instrument at the Centre for Advanced Microscopy at the Australian National University. Backscattered electron (BSE) images were collected, allowing the distinction of the different phases in the coatings and their textural relationships. Due to the roughness and fine grain size of some phases in the coatings, quantitative compositional analysis is not possible. Instead, we used Energy Dispersive Spectroscopy (EDS) with an 80-mm^2 silicon drift detector to collect qualitative elemental maps from the same areas where the BSE images were recorded. To increase the efficiency of element mapping, we increased the beam current to 1,000 pA by widening the condenser lens and reduced the spectrum processing time by 20%.

Surface phases and modification features observable in cross sections of the reacted glass substrates were analyzed with nanoscale secondary ion mass spectrometry (nanoSIMS), using a CAMECA nanoSIMS 50L instrument at the Centre for Microscopy, Characterization and Analysis, at the University of Western Australia. The samples were mounted in resin, polished and gold coated. We used a Hyperion (H200) oxygen ion (O^-) source, providing a spot size of 100 nm with a beam current of 12.5 pA and an ion impact energy of

Table 2
Phases Formed in the SO2-Basalt Glass Reactions at 700 °C

Sample composition	Redox buffer	T (°C)		t (hr)	Phases in the coating	Phases in the modified substrate
Fe-free basalt		700	$<T_g$	1	$CaSO_4$, $MgSO_4$, TiO_2	no crystallites
				24	$CaSO_4$, $MgSO_4$, TiO_2	no crystallites
Tholeiitic basalt	NNO−1.5	700	$<T_g$	1	$CaSO_4$, $MgSO_4$, Na_2SO_4, Fe_2O_3	no crystallites
				24	$CaSO_4$, $MgSO_4$, Fe_2O_3	no crystallites
	NNO	600	$<T_g$	24	$CaSO_4$, $MgSO_4$, Fe_2O_3	no crystallites
		700		1	$CaSO_4$, $MgSO_4$, Na_2SO_4, Fe_2O_3, Fe-Ti-(Al)-oxide	no crystallites
				24	$CaSO_4$, $MgSO_4$, Na_2SO_4, Fe_2O_3, Fe-Ti-(Al)-oxide	Fe-Na-pyroxene, Mg-pyroxene
		800	$>T_g$	1	$CaSO_4$, $MgSO_4$, Na_2SO_4, Fe_2O_3	SiO_2
	NNO+1	700	$<T_g$	1	$CaSO_4$, Na_2SO_4, $MgSO_4$, Fe_2O_3, Fe-Ti-(Al)-oxide	SiO_2
				24	$CaSO_4$, Na_2SO_4, Fe_2O_3, Fe-Ti-(Al)-oxide	SiO_2, Al_2O_3, Fe-Na-pyroxene, Mg-pyroxene
Alkali basalt	IW (NNO−5)	800	$>T_g$	1	$CaSO_4$, $MgSO_4$, $Na_2Ca(SO_4)_2$, Fe_2O_3, Fe3O4, Fe-Ti-(Al)-oxide	Mg-Fe-pyroxene, SiO_2
				96	$CaSO_4$, $MgSO_4$, $Na_2Ca(SO_4)_2$, Fe_2O_3, Fe_3O_4, Fe-Ti-(Al)-oxide	Mg-Fe-pyroxene
	NNO	600	$<T_g$	24	$CaSO_4$, Na_2SO_4, Fe_2O_3	not determined
		800	$>T_g$	1	$CaSO_4$, Na_2SO_4, Fe_2O_3, Fe_3O_4	not determined

Note. For each experiment, the phases in the surface coatings were determined using Raman spectroscopy and EDS (Figure 1), and the crystalline phases in the reacted substrates were inferred from nanoSIMS chemical maps (Figures 3–8).

16 keV. Maps of the isotopes ^{23}Na, ^{24}Mg, ^{27}Al, ^{28}Si, ^{40}Ca, ^{48}Ti, and ^{56}Fe were collected simultaneously in multicollection mode with a field of view of 50 μm^2 at a resolution of 512 × 512 pixels.

3. Results

3.1. Mineralogy of the Coatings

The coatings on the glasses and supercooled melts reacted with SO_2 include anhydrite ($CaSO_4$), $MgSO_4.nH_2O$, Na_2SO_4, glauberite ($Na_2Ca(SO_4)_2$), hematite (Fe_2O_3), magnetite (Fe_3O_4), and anatase (TiO_2). The coating assemblages are summarized in Table 2. Raman spectra show narrow bands (Figure 1) confirming that well-crystallized anhydrite ($CaSO_4$) is the most abundant phase in the coatings (using band positions reported by Liu et al., 2009).

Since our experiments were carried out in the absence of water, we expect that the $MgSO_4.nH_2O$ was initially anhydrous. Nonetheless, using the main Raman SO_4^{2-} stretching modes, we can identify three differently hydrated magnesium sulfate phases including $MgSO_4{\cdot}H_2O$ (kieserite), $MgSO_4{\cdot}2H_2O$ (sanderite), and $MgSO_4{\cdot}3H_2O$ (trihydrate; Wang et al., 2006). Despite placing the reacted glass samples in a desiccator immediately after taking them out of the gas-mixing furnace, Raman analysis was performed under air and so we suspect that hydration of $MgSO_4$ occurred after the experiments. This underlines the difficulty of appropriately handling gas-solid reaction products (Dalby et al., 2018; Palm et al., 2018) and the need to use a N_2 or Ar purge during analysis.

Sodium is incorporated in two different sulfates, including Na_2SO_4 and the mineral glauberite ($Na_2Ca(SO_4)_2$; Figure 1). The polymorph of Na_2SO_4 could not be identified unambiguously because of its poor crystallinity and occurrence in a mixture with Fe_2O_3 (Figure 1). Glauberite is observed only on the alkali basalt supercooled melt preequilibrated under highly reducing conditions (~NNO−5) and reacted with SO_2 at 800 °C (Table 2). Glauberite is identified by an intense band at 1,002 cm^{-1} in the Raman spectrum, which is distinct from anhydrite (1,016 cm^{-1}; Buzgar et al., 2009; Lopez-Reyes et al., 2014). The sulfate spectra collected using Raman tend to have a broad amorphous band, which suggests that the sulfate coatings are thinner than the penetration depth of the Raman laser, resulting in both the coating and the glass being probed simultaneously (Mernagh et al., 2018).

Oxide phases include hematite and magnetite (Zoppi et al., 2008), anatase (Tompsett et al., 1995) and a Fe-Ti-(Al)-oxide. Hematite occurs in the coatings of all experiments, as both large crystals with diameters of up to 10 μm, but also as very fine grained material intermixed with Na_2SO_4, such as on the basalt glass

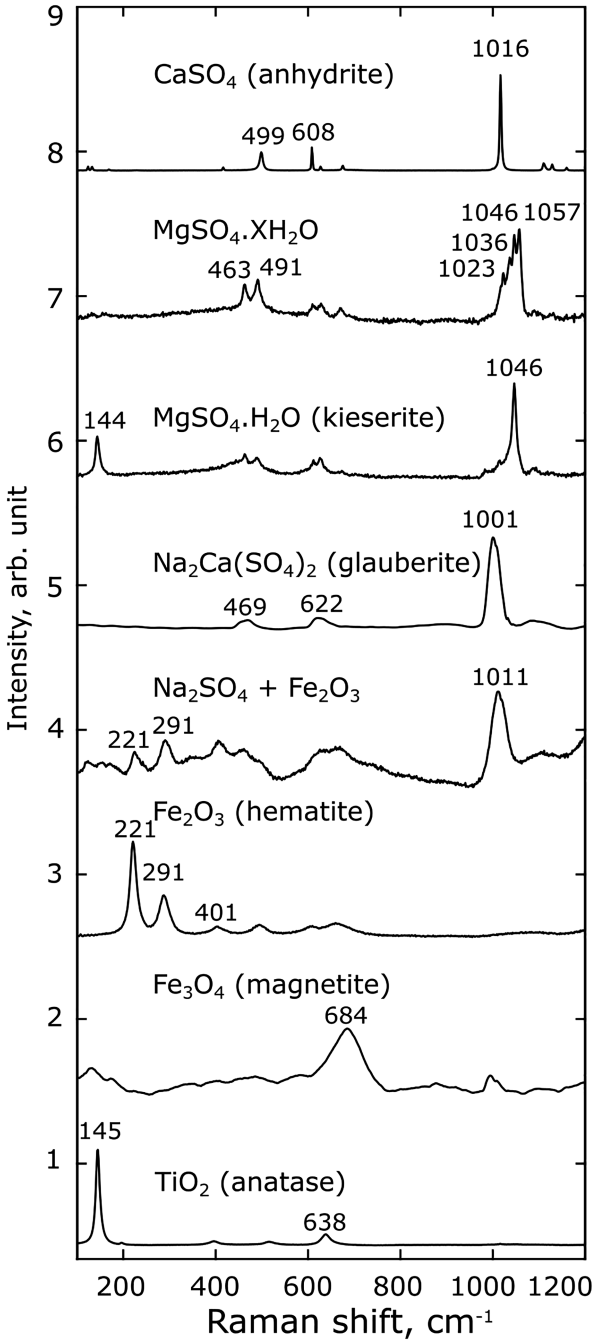

Figure 1. Raman spectra recorded on the coatings of the reacted basalt glasses. Anhydrite is well crystallized and its Raman spectrum shows sharp bands. The $MgSO_4$ is hydrated to various degrees. Based on the main Raman bands above 1,000 cm^{-1} we can identify the phases $MgSO_4{\cdot}H_2O$ (kieserite), $MgSO_4{\cdot}2H_2O$ (sanderite), and $MgSO_4{\cdot}3H_2O$ (trihydrate; Wang et al., 2006). Sodium is incorporated in the mineral glauberite as well as thenardite. Hematite occurs with Na_2SO_4 in a fine-grained mass, and also as wellcrystallized grains. Magnetite is only observed in the coating of the alkali basalt preequilibrated at NNO−5. The Ti-oxide (with some Al and Fe) is identified as anatase.

preequilibrated at NNO+1 (Figure 2f). The Raman spectrum collected for this mixture shows bands of hematite and Na_2SO_4 (Figure 1; Hapanowicz & Condrate, 1996). Magnetite was only observed on the alkali basalt supercooled melt that reacted at 800 °C, at NNO−5 and NNO (Table 2; Graves et al., 1988).

3.2. Textures and Chemistry of the Coatings

The SEM images show that the coatings are discontinuously mounded on the top of the glass substrates. Gaps in the coatings are evident in areas where high Si- and Al-counts are measured; these elements are immobile and remain at the surface of the substrate during reaction with SO_2 (Figures S2–S8 in the supporting information).

The textures of the surface coatings fall into two categories (Figure 2). First, fine-grained and equigranular coatings are found on the Fe-free basalt, the reduced alkali basalt preequilibrated at NNO−5 and the reduced tholeiitic basalt (NNO−1.5). Second, large anhydrite crystals, with lengths extending up to 100 μm (Figure 2), occur in the coatings on the more oxidized tholeiitic basalts (NNO and NNO+1) and the oxidized alkali basalt (NNO). Here we discuss the two types of textures separately.

On the Fe-free basaltic glass and the most reduced tholeiitic basalts (NNO −1.5), fine-grained $CaSO_4$ and $MgSO_4$ can be differentiated by their crystal habits (Figure 2) and the EDS maps of S, Ca, and Mg (Figures S2–S8). After reaction for 1 hr, the crystal habit of the $CaSO_4$ is poorly developed (Figures 2a and 2g), but as the grains mature with longer experimental durations (i.e., 24 hr), they establish facets (Fe-free basalt, Figure 2j) and grain-boundary triple-junctions, with dihedral angles of 120° (NNO−1.5, Figure 2d). The $MgSO_4$ grains are rounded, likely because the grains have taken up variable amounts of water after the experiments. In the BSE images (Figure 2) the $MgSO_4$ grains can further be identified by their darker gray shade. The grain sizes of the coatings on the Fe-free basalt and the reduced NNO−1.5 basalt are similar after 1 hr and 24 hr (Figure 2). The coatings on both of the latter glass substrates do not contain any Na_2SO_4 (Figures S1–S4).

The textures of the coatings on the SO_2-reacted reduced (~NNO−5) alkali basalt are similar to the fine-grained texture observed on the Fe-free basaltic glass, but with additional fine-grained glauberite and rounded hematite and magnetite crystals up to 20 μm in diameter. The sulfates are generally fine grained and the coating can be wrinkled and buckled in areas where the coating is thickest, due to lateral expansion of the coating (Renggli et al., 2019; Renggli & King, 2018).

The coatings on the more oxidized (NNO and NNO+1) basalts are dominated by large elongated $CaSO_4$ crystals with grain sizes of up to 100 μm in length (Figure 2). For the basalts preequilibrated at the NNO-buffer, the grain sizes are consistently larger on the reacted tholeiitic basalt compared with the alkali basalt (Figure 2). The coating on the surface of the reacted alkali basalt (NNO) is also more discontinuous (patchy) in comparison to the tholeiitic basalt.

The large $CaSO_4$ grains show a perfect cleavage perpendicular to the longest crystal axis (Figure 2). This cleavage plane corresponds to the (001) plane (Tröger, 2017), and hence the longest dimension of the elongated grains is the crystallographic *c* axis. Anhydrite has the largest thermal expansion coefficient along the crystallographic *c* axis, with a relative expansion of 2% from room temperature to 700 °C (Evans,

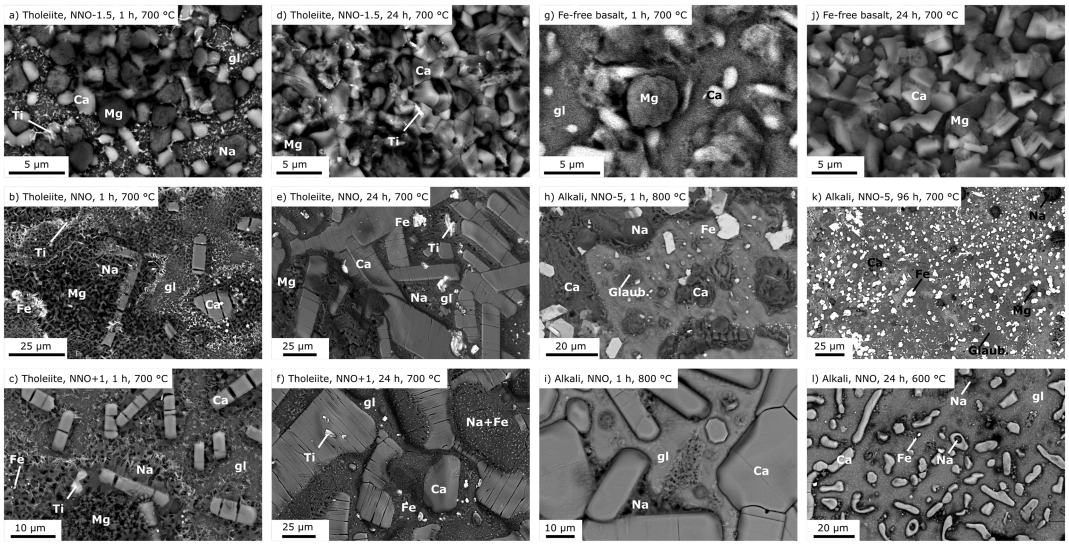

Figure 2. Backscattered electron images of the surface coatings on the basalt glasses reacted with SO_2 at 700 °C. Element symbols indicate the following phases: Ca = $CaSO_4$; Mg = $MgSO_4$; Na = Na_2SO_4; Fe = Fe_2O_3; Ti = TiO_2; Glaub = glauberite ($CaNa_2(SO_4)_2$; gl = basalt glass substrate. (a) Tholeiitic basalt preequilibrated at NNO−1.5, reacted for 1 hr at 700 °C. (b) Tholeiitic basalt preequilibrated at NNO, reacted for 1 hr at 700 °C. (c) Tholeiitic basalt preequilibrated at NNO+1, reacted for 1 hr at 700 °C. (d) Tholeiitic basalt preequilibrated at NNO−1.5, reacted for 24 hr at 700 °C. (e) Tholeiitic basalt preequilibrated at NNO, reacted for 24 hr at 700 °C. (f) Tholeiitic basalt preequilibrated at NNO+1, reacted for 24 hr at 700 °C. (g) Fe-free basalt reacted for 1 hr. (h) Alkali basalt preequilibrated at NNO−5, reacted for 1 hr at 800 °C. (i) Alkali basalt preequilibrated at NNO, reacted for 1 hr at 800 °C. (j) Fe-free basalt reacted for 24 hr at 700 °C. (k) Alkali basalt preequilibrated at NNO−5, reacted for 96 hr at 700 °C. (l) Alkali basalt preequilibrated at NNO, reacted for 24 hr at 600 °C.

1979). As the $CaSO_4$ crystals cool after removal from the furnace, they shrink, and the crystals split on the cleavage planes.

On the tholeiitic glass preequilibrated at NNO hydrated $MgSO_4$ forms large patches with diameters of up to 200 µm. On the most oxidized tholeiitic basalt glass (NNO+1), the coating formed during the 1-hr experiment contains distinct $MgSO_4$ grains, but the coating formed in the 24-hr experiment does not contain any $MgSO_4$ (Figure 2f). Figures 2j and 2e show that the textural features of $MgSO_4$ are affected by hydration after the experiments. Due to the volume increase of the magnesium sulfate caused by hydration, it now partially overlies the $CaSO_4$ crystals (Figure 2e).

Sodium sulfate forms fine needles which are commonly twinned and have grain sizes of less than 2 µm (Figure 2). On the reacted alkali and tholeiitic basalts (preequilibrated at the NNO-buffer) Na_2SO_4 is mainly observed in-between the $CaSO_4$ crystals and to a lesser degree associated with $MgSO_4$ (Figure S6). On the most oxidized tholeiitic glass (NNO+1) fine-grained Na_2SO_4 occurs in dense aggregates and is mixed with discrete, fine-grained Fe_2O_3 crystals (Figures 2f and S8), that are revealed by Raman spectra (Figure 1).

Hematite and anatase are clearly observed by their light gray hues in the BSE images (Figure 2), high iron and titanium counts in the EDS maps (Figuress S1–S8) and Raman spectra (Figure 1). The grain size of hematite ranges from <1 µm on the basalt glass preequilibrated at NNO−1.5 to 20 µm on the NNO glass (Figure 2). On the most oxidized glass (NNO+1) submicron Fe_2O_3 grains are associated with Na_2SO_4 aggregates (Figures 1, 2f, and S8). Anatase is less abundant than hematite, and grain sizes range from <1 to 10 µm.

In summary, the coating textures and mineral assemblages on the basalt glasses differ between (1) the Fe-free glass, the reduced (~NNO−5) alkali basalt and the most reduced tholeiitic basalt glass (NNO−1.5) and (2) the more oxidized tholeiitic basalt glasses (NNO and NNO+1). The assemblages are summarized in Table 2. In the Fe-free and reduced basalts (1), the coatings consist of equigranular grains of $CaSO_4$ and $MgSO_4$, with no significant textural differences observed between 1-hr- and 24-hr-long experiments. In the oxidized basalts (2), the coatings are dominated by large $CaSO_4$ crystals, which increase in size in the 24-hr experiments

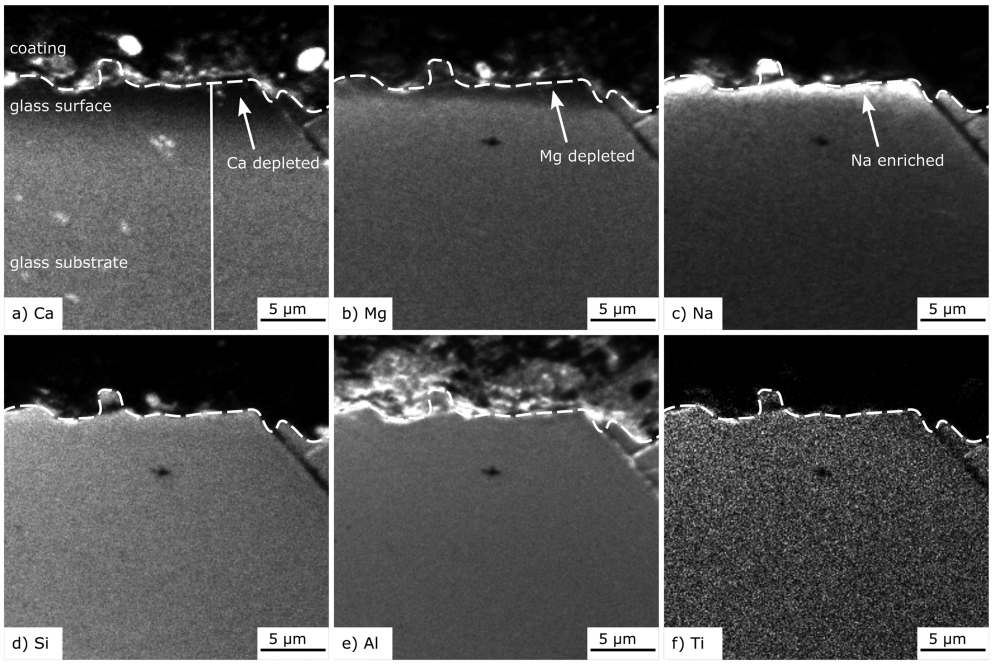

Figure 3. NanoSIMS count map of a cross section through the Fe-free basalt reacted with SO_2 at 700 °C for 24 hr. The stippled line shows the interface below which is the glass substrate. White indicates high count rates, black indicates low count rates. (a) Ca, (b) Mg, (c) Na, (d) Si, (e) Al, (f) Ti. The white line on the Ca map indicates the position of the profile shown in Figure 8d.

compared with the 1-hr experiments (Figure 2). In the 24-hr experiments $MgSO_4$ and Na_2SO_4 (Table 2) fill in the space between and occasionally overgrowing onto the large $CaSO_4$ crystals. This suggests that Na_2SO_4 and $MgSO_4$ sulfates nucleate or grow, at least partially, after $CaSO_4$. In the case of $MgSO_4$, postexperiment hydration has likely affected our interpretation of its texture.

3.3. Chemistry of the Glass Substrate in Cross Section

Chemical element maps of cross sections measured using nanoSIMS reveal crystallites and chemical zones in the reacted basalts (Figures 3–7). The nanoSIMS maps show relative increases and decreases in count rates, which correlate with the relative concentrations of the elements. The figures are annotated to highlight features described in the text. Figure 8 shows profiles across the nanoSIMS maps, highlighting relative enrichments and depletions in the major elements from the surface to the modified basalt glass substrates.

In some cross sections of the reacted samples, the coating is poorly preserved. In these cases, the coating was lost when the cross sections were cut, polished, and embedded in epoxy. For example, the coating on the Fe-free basalt glass is mostly lost (Figure 3), whereas it is well-preserved on the most oxidized (NNO+1) tholeiitic basalt glass (Figure 6). In this case, the nanoSIMS map (Figure 6) shows a sulfate coating on the glass surface with a thickness of ~8 µm, predominantly consisting of $CaSO_4$ with some Na-rich sulfate. Iron oxides, Ti-oxides, and Fe-Ti-oxides are also observed in the coating layer (Figure 6). At depth, with a distance of 10–50 µm from the surface depending on the sample, the glasses remain homogeneous, unreacted, and crystal free.

The Fe-free basaltic glass substrate shows the least amount of modification after reaction with SO_2 for 24 hr at 700 °C (Figure 3). Calcium and Mg are depleted at the glass surface (Figures 3a, 3b, and 8d). The concentration of Ca increases into the glass substrate over a distance of 5 µm, whereas Mg increases occur over a shorter distance of ~2 µm. Sodium is enriched at the surface to a depth of 2–5 µm (Figure 8d). The depletion of Ca and Mg in the glass substrate correlates with the observation of $CaSO_4$ and $MgSO_4$ in the sulfate coating, whereas Na_2SO_4 is not observed and hence Na is retained in the near-surface glass substrate. There is no change in Si, Al, and Ti in the glass substrate (Figures 3d–3f). No sharp peaks are observed in the major element profiles (Figure 8d), which suggests that no crystallites have nucleated on

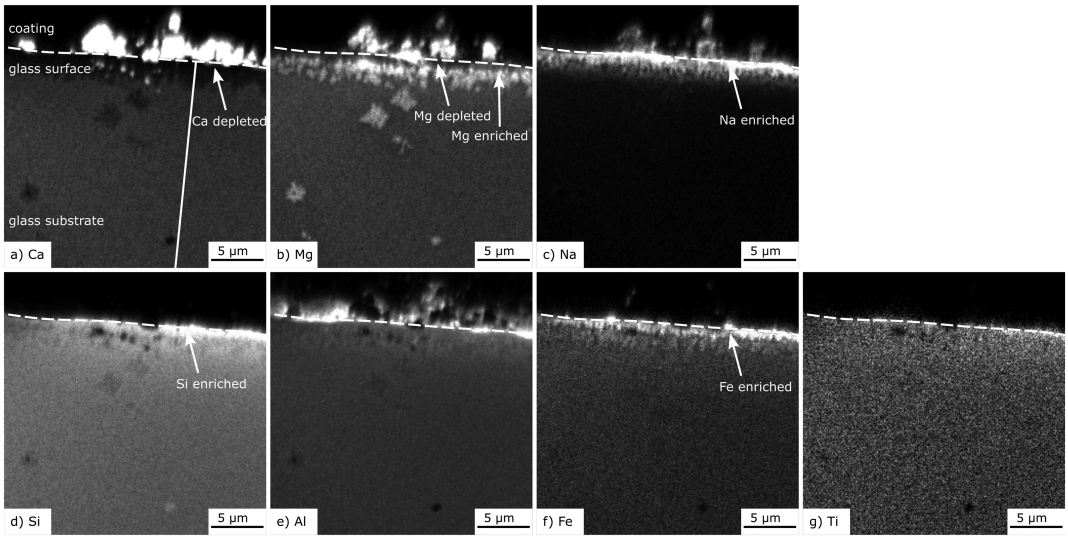

Figure 4. NanoSIMS count map of a cross section through the tholeiitic basalt, preequilibrated at NNO−1.5 and reacted with SO_2 at 700 °C for 24 hr. The stippled line shows the interface below which is the glass substrate. White indicates high count rates, black indicates low count rates. (a) Ca, (b) Mg, (c) Na, (d) Si, (e) Al, (f) Fe, (g) Ti. The white line on the Ca map indicates the position of the profile shown in Figure 8a.

the 100-nm scale. The slopes in the profiles with increasing distance from the surface are an artifact from the semiquantitative nanoSIMS analysis.

The tholeiitic glass preequilibrated at NNO−1.5 is modified in a similar manner to the Fe-free basalt glass (Figure 4). Calcium is depleted at the surface of the glass substrate to a depth of ~3 µm (Figure 4a) and Na is enriched in the same zone at the glass surface (Figures 4c and 8a). Magnesium-rich crystals are present in the reacted basaltic substrate to a depth of 20 µm (Figure 4b), but the highest density zone of Mg-rich crystallites occurs within 3 µm of the surface. The largest crystallites have diameters of up to 2 µm. Silicon- and Fe-bearing crystallites form in the glass substrate within 1–3 µm of the surface (Figures 4d and 4f).

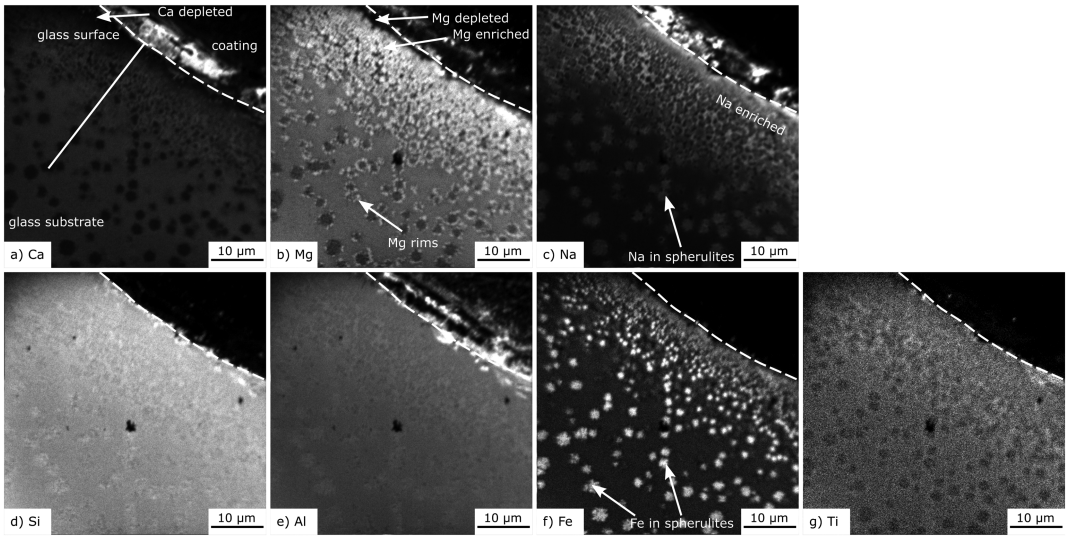

Figure 5. NanoSIMS count map of a cross section through the tholeiitic basalt, preequilibrated at NNO and reacted with SO_2 at 700 °C for 24 hr. The stippled line shows the interface below which is the glass substrate. White indicates high count rates, black indicates low count rates. (a) Ca, (b) Mg, (c) Na, (d) Si, (e) Al, (f) Fe, (g) Ti. The white line on the Ca map indicates the position of the profile shown in Figure 8b.

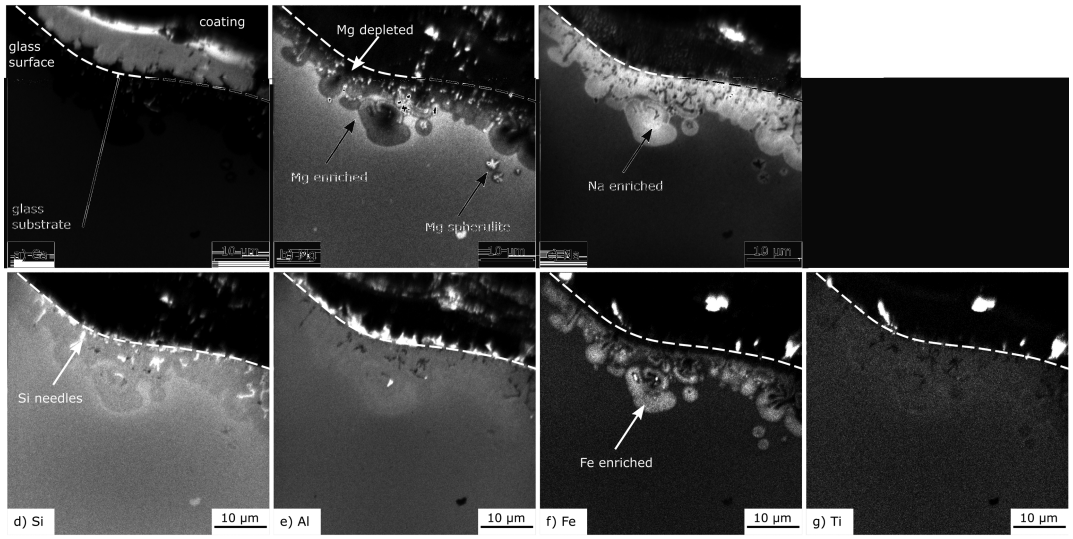

Figure 6. NanoSIMS count map of a cross-section through the tholeiitic basalt, preequilibrated at NNO+1 and reacted with SO_2 at 700 °C for 24 hr. The stippled line shows the interface below which is the glass substrate. White indicates high count rates, black indicates low count rates. (a) Ca, (b) Mg, (c) Na, (d) Si, (e) Al, (f) Fe, (g) Ti. The white line on the Ca map indicates the position of the profile shown in Figure 8c.

In the reacted tholeiitic glass preequilibrated at NNO (Figure 5), Ca is depleted at the surface to a depth of <10 µm (Figure 5a). In comparison, Na becomes increasingly enriched toward the glass surface from a depth of 20 µm (Figure 5c). Nucleation of Fe-, Na-, and Mg-rich spherulites is observed throughout the sample, with decreasing numbers and increasing grain sizes from the surface toward the interior of the glass (Figures 5b, 5c, 5f, and 8b). The crystals have Fe-rich cores and Na-concentrations are elevated throughout the spherulites. This is evident when comparing Figures 5c and 5f, where high Na and Fe count rates are observed at a depth of more than 15 µm from the surface of the reacted glass. We interpret the larger spherulites with diameters of up to 3 µm as pyroxenes (e.g., $NaFe^{3+}Si_2O_6$, aegirine). They are surrounded by Mg-rich material, which may correspond to $MgSiO_3$ (enstatite or clinoenstatite). The Mg-rich rims become

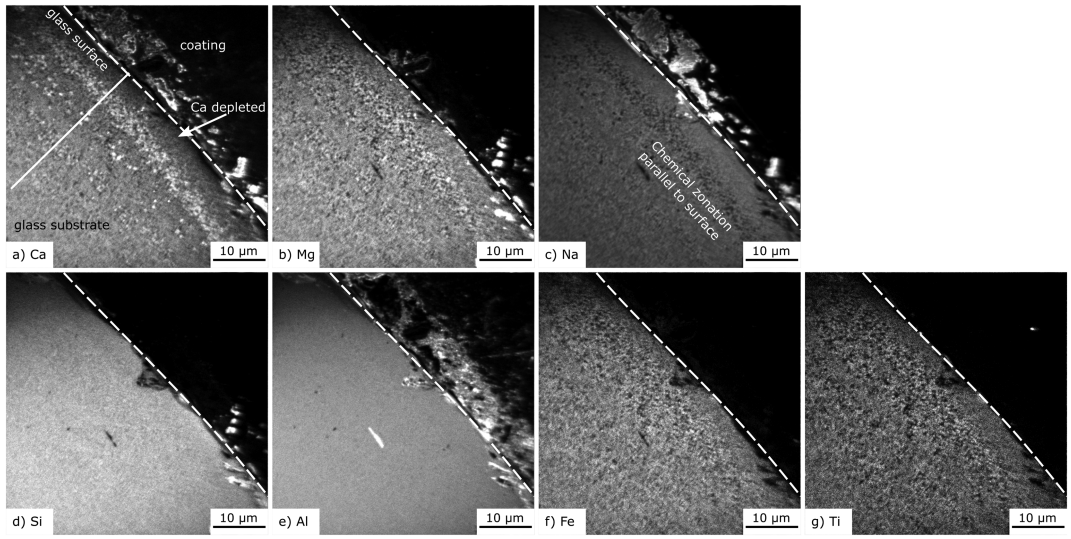

Figure 7. NanoSIMS count map of a cross section through the alkali basalt, preequilibrated at NNO−5 and reacted with SO_2 at 800 °C for 1 hr. The stippled line shows the interface below which is the glass substrate. White indicates high count rates, black indicates low count rates. (a) Ca, (b) Mg, (c) Na, (d) Si, (e) Al, (f) Fe, (g) Ti. The white line on the Ca map indicates the position of the profile shown in Figure 8e.

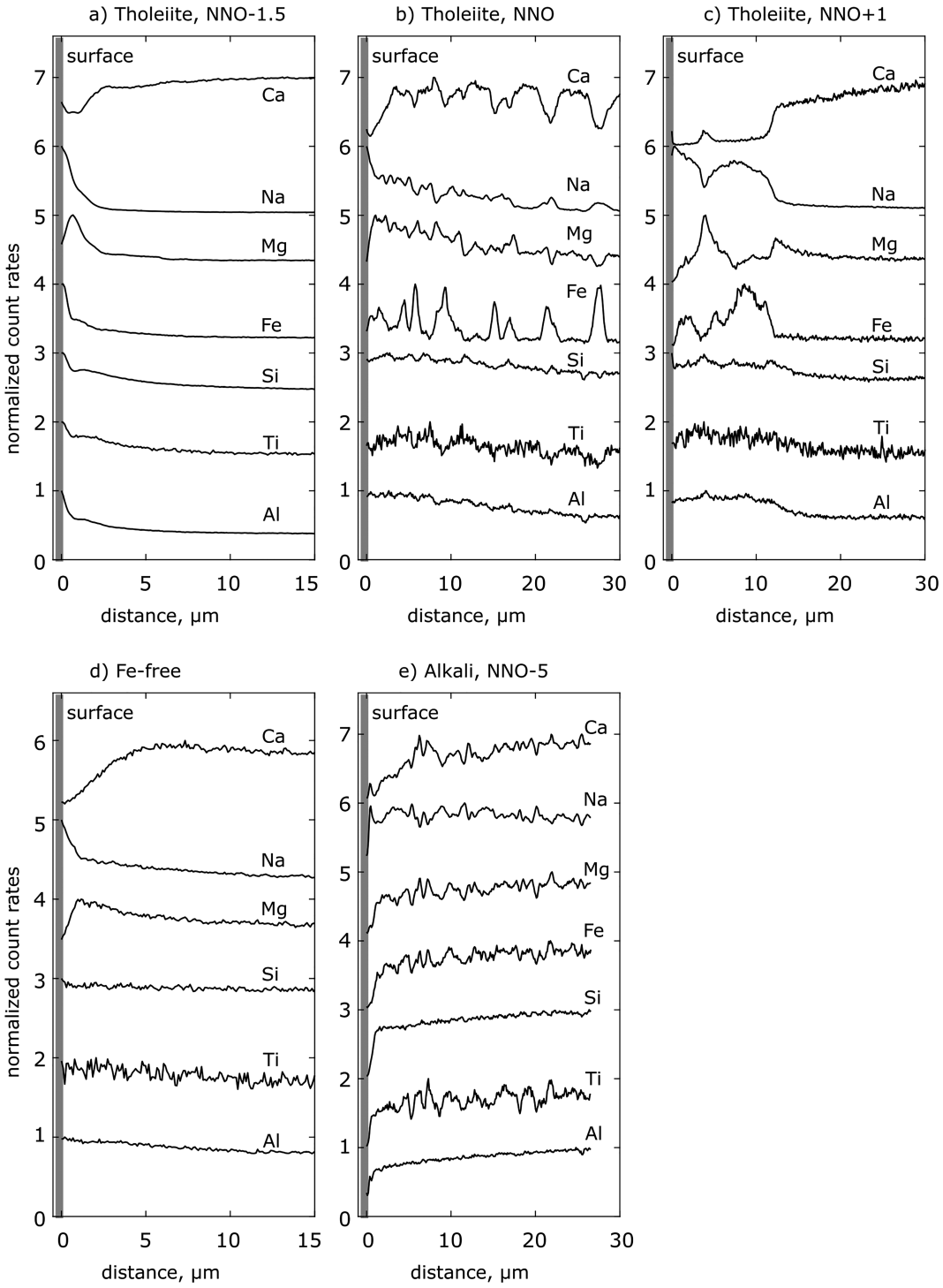

Figure 8. Normalized nanoSIMS profiles from the surface into the reacted substrates of the basalt glasses reacted at 700 °C for 24 hr. The positions of the profiles are indicated on the Ca maps of the respective nanoSIMS analysis (Figures 3a, 4a, 5a, 6a, and 7a). Peaks in the basalt glass substrates indicate the occurrence of crystallites. (a) Tholeiite NNO−1.5; (b) tholeiite NNO; (c) tholeiite NNO+1; (d) Fe-free basalt; (e) alkali NNO−5.

increasingly discontinuous with distance from the glass surface. Calcium counts are low in the spherulitic crystallites and Si, Al, and Ti show minor variations (Figure 8b).

The modification of the most oxidized tholeiitic basalt glass (NNO+1) differs from the other glasses in its texture and the composition of the nucleated phases (Figure 6). Calcium is strongly depleted at the surface to a depth of 12 μm (Figures 6a and 8c). Mushroom-shaped features, defined by stong gradients in Mg, Na, and Fe, are observed up to 20 μm from the glass surface. These are highly enriched in Na and Fe and include a number of different crystallites (Figures 6c and 6f). Sodium is enriched throughout the modified zone, whereas Fe is depleted within 1.5 μm of the glass surface and enriched further into the glass (Figures 6c and 6f). Magnesium is enriched around the mushroom-shaped modification features but is also depleted within ~2 μm from the surface (Figure 6b). Crystals are evident as peaks in the nanoSIMS line profile (Figure 8c), similar to the NNO glass (Figure 8b), and include Mg-rich spherulites surrounded by Fe- and Na-rich material, Fe-rich crystallites (Figure 6f) and SiO_2 needles (Figure 6d), and Al-rich material (Figure 6e), possibly Al_2O_3. The different nanoSIMS figures (Figures 3–7) show that the Al-rich material fills the gap between reacted glass substrate, coating phases, and the surrounding epoxy resin. This textural setting could be explained by it being derived from either contamination or as a reaction product. Thermodynamic calculations suggest that Al_2O_3 could form as a reaction product, and it has been observed on the surface of pyroxene reacted with SO_2 (King et al., 2018). We sought to determine if the Al_2O_3 could be detected on the surface of an unpolished sample by Raman spectroscopy or scanning electron microscopy, rather than just in the polished section. The surface analyses did not reveal the Al_2O_3 phase, and this might be due to it either not being present or alternately, below the detection limits of the techniques since nanoSIMS indicates that it is found in very thin layers. At this time, we are not able to identify the source of the Al-enrichment as being either contamination or a reaction product.

The nanoSIMS maps of the reduced alkali basalt supercooled-melt (~NNO−5) reacted with SO_2 at 800 °C for 1 hr show the presence of Ca and Na in the coating, which agrees with the observation of the mineral glauberite ($Na_2Ca(SO_4)_2$; Figures 1 and 7). The basalt is modified to a depth greater than 50 μm. We propose that modification and crystallization results from both reaction with SO_2 and from heating the silicate glass above its glass transition temperature. Near-surface crystallization of supercooled melts reacting with SO_2 was previously observed in experiments in the anorthite-diopside system (Renggli et al., 2019). The modified alkali basalt shows a stratification of major element enrichment (Figures 7 and 8e). This is best observed for Ca, Mg, and Na, which are the most mobile elements in this reaction, as observed in their enrichment in the coating (Figure 2). Crystallization products in this basalt were previously identified as orthopyroxene (hypersthene; Palm et al., 2018).

In summary, the observed modification of the basalt glasses after 24 hr of reaction with SO_2 extends into the glass substrate to a depth of less than 5 μm from the surface in the case of the Fe-free and the NNO−1.5 glasses (Figures 8d and 8e). The more oxidized glasses are modified to a depth of ~20 μm (NNO+1) to more than 50 μm (NNO) from the surface (Figures 8b and 8c). The alkali basalt supercooled melt preequilibrated at NNO−5 is modified to a greater depth due to the reaction above T_g, which allows the rapid crystallization during the experiment. The formation of sulfates on the glasses is reflected by a strong depletion of Ca close to the surface of the glass substrate. Magnesium and Fe are also depleted near the glass surface, whereas Na is enriched near the surface of the glass substrate in the tholeiite glass experiments. Crystallites in the modified Fe-bearing basalt glasses are rich in Mg and Fe, with some Na incorporated in the Fe-rich crystallites. We were not able to directly identify the minerals, but the nanoSIMS maps suggest that they are $NaFe^{3+}Si_2O_6$ (aegirine) and $MgSiO_3$ (enstatite or clinoenstatite). Hypersthene was previously identified in alkali basalt glass that reacted with SO_2 (Palm et al., 2018). The reaction products in the glasses were caused by the reaction with SO_2 at high temperatures. The unreacted materials were homogenous and crystal free (e.g., Figures 3–8 show homogeneous composition at depth). Upon annealing of the glasses at 800 °C in air we did not observe the chemical alteration textures observed in the SO_2 reaction experiments (supporting information).

4. Discussion

We argue that the formation of phases in the coating is controlled by the role of the cations (Ca^{2+}, Mg^{2+}, Na^{+}, $Fe^{2+/3+}$) in the glass structure and their ability to migrate to the glass surface (mobility). Calcium diffusion has previously been suggested as the rate-limiting factor in the reaction between SO_2-bearing gas and glassy ash, which forms $CaSO_4$ (Ayris et al., 2013; Delmelle et al., 2018). The mineralogy of the crystallites

in the substrate is controlled by the locally changing composition, which is due to the loss of Ca, Mg, Na, and Fe to the coating. First, we discuss the basaltic glass structure and how it may affect the reaction mechanism. We then discuss how the reaction oxidizes the Fe-bearing basalt glasses and supercooled melts, resulting in an increase in Fe^{3+}/Fe_{tot}, and present a model for the reaction mechanism. We present thermodynamic calculations showing the predominance of Fe, Na, Ca, and Mg phases, including oxides, sulfides, and sulfates, as a function of $\log fO_2$ and $\log fSO_2$ in the gas phase and relate our experiments to gas-solid processes that occur in natural systems on planetary bodies including Earth, Venus, Mars, Io, the Moon, and Mercury.

4.1. Role of the Glass Structure and Redox State on Reaction Products

Glass structure and composition have been shown to be important controls on the reaction with SO_2 (Ayris et al., 2013; Renggli et al., 2019; Renggli & King, 2018). In the structure of a silicate glass, Si^{4+}, Ti^{4+}, Fe^{3+}, and Al^{3+} cations are tetrahedrally (T)-coordinated by O^{2-} ions. These tetrahedral building blocks form a network with short- to medium-range order, but no long-range order (Mysen & Richet, 2005). The O^{2-} ions may either bond to two network forming T-cations, forming T-O-T bonds and acting as bridging oxygens (BO), or they may link a T-cation with a network modifying cation (M; e.g., Na^+, K^+, Mg^{2+}, Ca^{2+}, and Fe^{2+}), forming T-O-M bonds and acting as nonbridging oxygens (NBO). The number of nonbridging oxygens per tetrahedrally coordinated cation (NBO/T) describes the degree of polymerization of the amorphous network (Mysen & Richet, 2005). Tetrahedrally coordinated Al^{3+} and Fe^{3+} cations further require charge balancing by a monovalent or divalent cation as they are negatively charged ($[M^{3+}O_4]^-$). Alkali earths in particular may change their role in the glass structure and act as charge compensators, instead of network modifiers (Angeli et al., 2000; Le Losq et al., 2014; Le Losq & Neuville, 2017; Neuville & Mysen, 1996).

In more reduced glasses (~NNO−5, NNO−1.5, and NNO) the Na^+ concentration is sufficient to charge balance all tetrahedrally coordinated Fe^{3+} cations ($Fe^{3+}/Na^+ < 1$; Table 1). However in oxidized glasses, alkalis are not sufficient to completely charge balance all of the tetrahedrally coordinated trivalent cations in the glass, and some divalent cations (Ca^{2+}, Mg^{2+}, Mn^{2+}) are required for charge compensation. The need for charge compensation increases in the more oxidized glasses (NNO+1), where the abundance of tetrahedrally coordinated Fe^{3+} is higher ($Fe^{3+}/Fe_{tot} = 0.79$ for the tholeiitic basaltic glass preequilibrated at NNO+1).

The reaction of SO_2 with Fe-bearing basaltic glass is an example of a surface-mediated reaction that includes oxidation (King et al., 2018). Because sulfur is a polyvalent element (S^{2-}, S^-, S^0, S^{4+}, S^{6+}), the redox state of both the gas and solid reactants play a role in the reaction. Here, we assume that the SO_2 used in the experiments is pure and dissociates at equilibrium to form other gas species including S_2, S_3, SO_3, SO, S_2O, and O_2 (Renggli & King, 2018; Zolotov & Fegley, 1999). Using a Gibbs Free Energy minimization calculation of the equilibrium dissociation of SO_2, the fO_2 of the gas is $\log fO_2 = -12.1$ at 700 °C and 1 bar, equivalent to 4.2 log units above the NNO-buffer (O'Neill & Pownceby, 1993). Consequently, the SO_2 reaction with the more reduced basalts (NNO−5 to +1, Table 2) imposes a redox gradient.

In a H-free system where a silicate glass reacts with an oxidizing gas, this electrochemical potential gradient is most efficiently dissipated by the rapid diffusion of electron holes into the glass to oxidize Fe^{2+} to Fe^{3+}. The inward diffusion of the electron holes is charge compensated by the counterdiffusion of Ca and Mg. This mechanism is explored by Cooper and coworkers (Cook & Cooper, 2000; Cooper, 2020; Cooper et al., 1996). They show that multivalent element-bearing aluminosilicate glasses act as semiconductors for electron holes, allowing their rapid diffusion. In this oxidation mechanism, the charge-compensating diffusion of Ca^{2+} and Mg^{2+} is the rate-limiting step. At the glass surface, Ca^{2+} and Mg^{2+} form MgO and CaO coatings in such an oxidation reaction (Cook & Cooper, 2000; Cooper, 2020; Cooper et al., 1996). Finally, the oxidized Fe^{3+} atoms require charge compensation if they are tetrahedrally coordinated, which results in the development of a Na-front at the oxidation front in the glass (Burkhard, 2001; Cook et al., 1990; Cook & Cooper, 2000). We observe a similar Na-front in the nanoSIMS maps and profiles obtained from our experiments (Figures 3–8), suggesting that this oxidation mechanism operates in our experiments. The nanoSIMS maps of a cross section of the reacted tholeiitic basalt (e.g., preequilibrated at NNO+1; Figure 6) show correlations between Fe-enrichment and Na-enrichment in the near-surface glass substrate. In these areas, Fe is likely present as Fe^{3+} and charge compensated by Na^+.

We argue that the new minerals observed both on the surface and within the basalt glasses reacted with SO_2 (Figures 3–8) are reaction products of the gas-solid reaction. To demonstrate the cause of the alteration is not the exposure to high temperatures we conducted an annealing experiment at 800 °C in air, without SO_2. A tholeiitic glass preequilibrated at NNO was kept at 800 °C in air for 24 hr (Figure S1). In cross section, the annealed glass shows no changes from the original material: it is homogeneous and crystal free. At the surface we observed micron-sized crystals of CaO and MgO, which is in agreement with previous studies investigating the oxidation of basaltic glasses (Cook & Cooper, 2000; Cooper, 2020; Cooper et al., 1996). Our experiments do not show any evidence for CaO and MgO, instead Ca and Mg sulfates. Both experiments are evidence for the diffusion of Ca and Mg in the glass toward the surface during annealing (as described by Renggli & King, 2018).

4.2. Sulfate Formation

The sulfate-forming cations Ca, Mg, and Na are mobilized and concentrated in surface coatings by two different mechanisms. First, as discussed above, the basalt oxidation mechanisms first proposed by Cook et al. (1990) results in the formation of CaO and MgO coatings on the glass surface. In the presence of SO_2 these alkaline earth oxides react at the surface of the glass to form sulfates (see equation (1)). Second, the chemisorption reaction of SO_2 with the glass surface imposes a chemical potential gradient from the surface to the interior of the glass and mobilizes the sulfate-forming cations to the surface. Both mechanisms are linked and cannot be separated, but the overall rates are limited by the diffusivities of the cations (Renggli & King, 2018). As the near-surface glass becomes increasingly depleted in the sulfate-forming cations the diffusivities change and the overall reaction rate does not remain constant. Furthermore, the changes in the glass composition result in the formation of SiO_2 and other crystallites that can armor the surface of the reactant, as observed in our experiments (Figures 3–8). This crystallization below the glass surface further limits the diffusion of the sulfate-forming cations to the surface and reduces the overall reaction rate.

Iron present at the surface of the glass is oxidized by SO_2 to form Fe-oxide minerals (e.g., hematite and magnetite). A titanium-rich oxide mineral, anatase (TiO_2), was also identified as a reaction product present in the coatings formed on the Fe-free and tholeiitic basalts reacted with SO_2. This is evidence that Fe and Ti may diffuse to the surface of the coating as the reaction progresses. The mineralogy of the Fe-oxide minerals formed is dependent on the temperature and gas partial pressure—particularly fO_2—of the experiment (Renggli & King, 2018; Figure 9); magnetite is only present in the 800 °C experiments on Fe-bearing basalts.

Thermodynamic calculations of the reaction between SO_2 and silicate minerals produce equilibrium assemblages of sulfates, aluminosilicate phase(s), metal oxides, and S_2 gas (King et al., 2018). In nature, complete reaction and attainment of equilibrium between minerals or glasses and SO_2 is unlikely and only occurs locally. For example, in the subvolcanic environment, sulfate veins form via the reaction of SO_2 with volcanic rocks over length scales of millimeters to meters (Casas et al., 2019; Henley et al., 2015, 2017; Henley & Seward, 2018). More extensive reaction is limited by mass transport of cations in the reacted solids, transport of SO_2 through veins and pore space, overall availability of SO_2 to the reaction, transport of S_2 in the system, and the lifetime of the volcanic system. In explosive volcanic eruptions the reaction is limited by the short lifetimes of high-temperature plumes of seconds to few minutes (Ayris et al., 2013), even though SO_2 is available in excess and the surface area of the fine-grained volcanic ash is large and favorable for the reaction.

Similar to nature, it was not possible to attain equilibrium conditions in the experiments within reasonable timescales. Instead, our observations show a snapshot of the reaction products on the way to equilibrium and represent what we expect in nature. Even in the coating at the surface equilibrium is not attained. The gas-solid reaction occurs in an open system at the glass surface, where SO_2 is continuously transported to the surface and reduced S-gas is removed (equation (1)). Similarly, the sulfate- and oxide-forming elements Ca, Mg, Na, Fe, and Ti diffuse to the reaction interface at changing rates throughout the experiment.

4.3. Implications for the Inner Planets, the Moon, and Io

In our experiments we varied the redox state of the basalt glass starting materials, but we did not vary the composition of the reacting gas phase. Here, we use thermodynamic calculations to address the effect of different fO_2 and fSO_2 on the stabilities of sulfate, sulfide, and oxide compounds of Fe, Na, Ca, and Mg. Figure 9 shows predominance plots of the prevailing phases in the systems Fe-S-O, Na-S-O, Ca-S-O, and Mg-S-O at

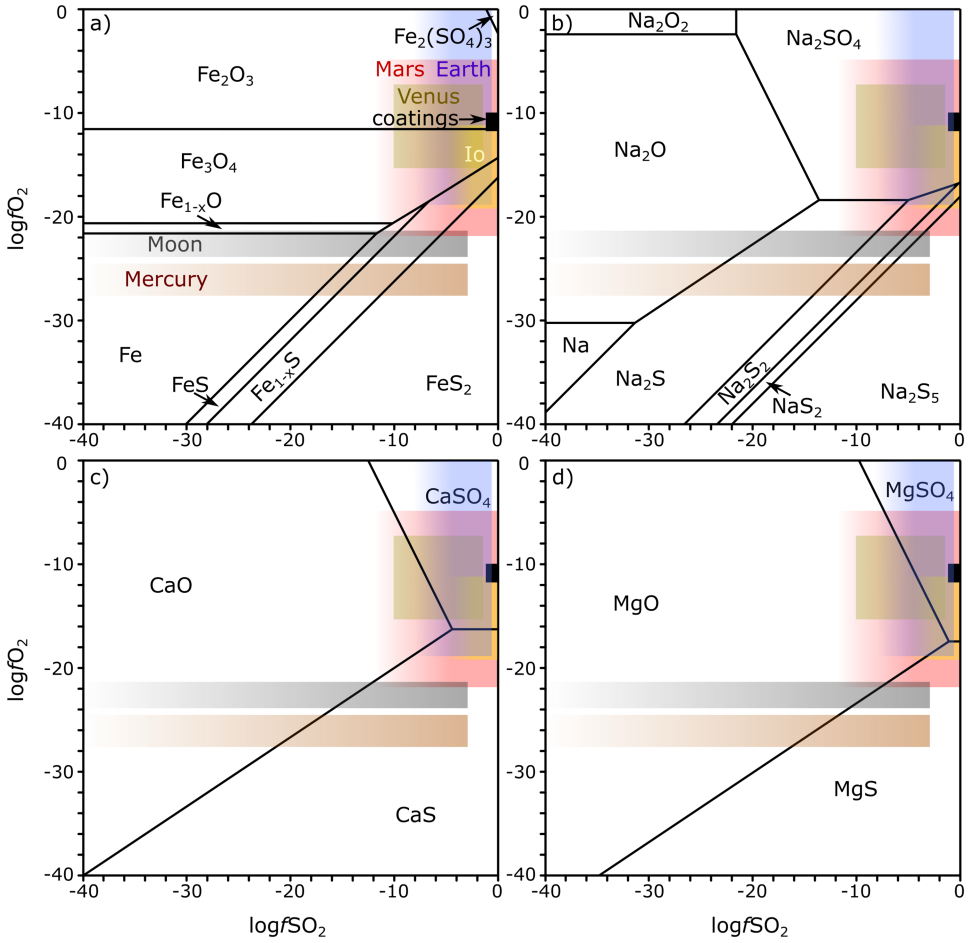

Figure 9. Phase predominance diagrams as a function of fSO_2 and fO_2 at 700 °C and 1 bar for the systems (a) Fe-S-O, (b) Na-S-O, (c) Ca-S-O, (d) Mg-S-O. The estimated SO_2 and O_2 fugacities in hot volcanic and atmospheric gases of different planetary bodies are marked in color. Blue: Earth (Ballhaus, 1993; Carmichael, 1991; Oppenheimer et al., 2011); red: Mars (Gaillard et al., 2013; Gaillard & Scaillet, 2009; Hirschmann & Withers, 2008); orange: Venus (Fegley et al., 1997; Vandaele et al., 2017); yellow: Io (Zolotov & Fegley, 1999; Zolotov & Fegley, 2000); gray: Moon (Renggli et al., 2017; Rutherford & Papale, 2009); brown: Mercury (Kerber et al., 2009; McCubbin et al., 2012; Zolotov, 2011). The black box shows the theoretical equilibrium conditions of the reaction with SO_2.

700 °C and atmospheric pressure, based on minimum Gibbs energies calculated using the program HSC9 by Outotec (Roine, 2015). The theoretical equilibrium condition in our experiments falls in the predominance fields of Fe_2O_3, Na_2SO_4, $CaSO_4$, and $MgSO_4$ (Figure 9), confirming the stability of the phases formed in the experiments.

The oxygen fugacity of terrestrial planetary bodies encompass a range of almost 30 orders of magnitude at their surfaces. We overlay estimated present and past SO_2 and O_2 fugacities of magmatic systems and atmospheric compositions over the phase predominance plots (Figure 9). This allows us to make predictions on the stability of sulfate, sulfide, and oxide phases of Fe, Na, Ca, and Mg on the surfaces of these planetary bodies, where reactions with S-bearing gases occur, assuming 1 bar of pressure.

On Earth, magmatic oxidation states range from NNO−3 to NNO+5 (Ballhaus, 1993; Carmichael, 1991; Oppenheimer et al., 2011). We extend the estimated field for Earth to higher fO_2 because S-bearing gases can mix with air to become more oxidizing. These conditions largely fall in the stability field of hematite and magnetite, Na-, Ca-, and Mg-sulfates in S-rich environments and Na-, Ca-, and Mg-oxides in S-poor systems. This agrees very well with the range of phases that we observed in the experiments (Figure 1) and that are predicted by the predominance plots (Figure 9). The limits of fSO_2 are more difficult to establish. The

highest observed SO_2 abundance in a volcanic gas on Earth is 0.21 mole fractions are from the Kilauea lava lake (Gerlach, 1980). As meteoric water is entrained in volcanic gas prior to eruption, H_2S becomes more abundant (Henley & Seward, 2018) and SO_2 abundances may drop below 10^{-4} mole fractions.

Magmas on Mars are more reducing than on Earth with fO_2 estimates ranging from slightly below NNO−5 to NNO (Castle & Herd, 2017; Gaillard et al., 2013; Gaillard & Scaillet, 2009; Hirschmann & Withers, 2008). Yet the atmosphere is oxidizing ($\log fO_2 \sim -5$) resulting in abundant oxidized hematite (King & McSween, 2005; Morris et al., 1989), suggesting that redox conditions in gas-solid reactions on Mars's surface could have been more oxidizing. Gaillard and Scaillet (2009) suggested SO_2 abundances of up to 0.1 mole fractions in a martian volcanic gas. Lower limits may be significantly below 10^{-4} mole fractions in an early Martian volcanic gas (Gaillard & Scaillet, 2009). Martian conditions fall in the stability fields of sulfates and oxides, but Na-, Ca-, and Mg- sulfides could occur in the lower range of redox conditions suggested for magmatic processes (Figure 9). Implications of these and other experiments for the fine material on Mars is the topic of ongoing work.

The oxygen fugacity of primary basalts on Venus is unknown and its atmosphere ranges from ~NNO+1 to ~NNO+9 (Fegley et al., 1997; Vandaele et al., 2017) which falls in the range of conditions estimated for Earth and Mars (Figure 9). The modern atmosphere of Venus contains ~150 ppm SO_2 and S-rich deposits on the surface likely formed via reactions between SO_2 and the basaltic surface (Zolotov, 2018, and references therein). The high S-abundance on the surface suggests that concentrations in volcanic gases and the atmosphere may have exceeded modern concentrations in the past (Zolotov, 2018). Zolotov (2018) discusses the stabilities of different rock-forming silicates, sulfates, sulfides, and carbonates at modern pressure and temperature conditions on Venus in more detail, suggesting that pyrite may be stable and that anhydrite is the only stable sulfate on the surface. For example, due to the presence of C-bearing species Mg forms carbonates instead of sulfates and the most stable Na-compound is albite (Zolotov, 2018).

Volcanic plumes on Io are S-rich and primarily consist of SO_2 and S_2 with oxidation states of NNO−3.3 to NNO+4 (Zolotov & Fegley, 1999, 2000). These conditions span the stability fields of sulfates and sulfides (Figure 9). At the more reducing S_2-rich conditions (<NNO) Fe, Na, Ca, and Mg may be stable as sulfides on Io.

The Moon and Mercury are significantly more reducing than the other planetary bodies discussed here, with redox conditions below the iron-wüstite buffer (~NNO−5.3; Rutherford & Papale, 2009;Kerber et al., 2009 ; McCubbin et al., 2012 ; Zolotov, 2011). Due to the lack of atmospheres and modern volcanic gases on both bodies, estimates for SO_2 concentrations are more difficult. Lunar volcanic gas models suggest that SO_2 may have occurred at up to 10^{-3} mole fractions (Renggli et al., 2017). Reactions between such a S-rich gas and the lunar regolith may have contributed to the formation of volatile-rich rocks such as the Apollo 16 "rusty rock," which contains sulfides and chlorides (Day et al., 2017; Shearer et al., 2014). In addition to Fe-sulfides, Na-, Ca-, and Mg-sulfides may also be stable at these conditions (Figure 9). Mercury is assumed to be more reducing than the Moon with conditions of NNO−8 to NNO−11 (Kerber et al., 2009; McCubbin et al., 2012; Zolotov, 2011). High S-abundances were observed on Mercury (Nittler et al., 2011; Starr et al., 2012; Weider et al., 2012). In Figure 9 we use $\log fSO_2$ estimates of the Moon for Mercury, and sulfur-bearing volcanic gas species have likely contributed to eruptive processes on Mercury (Kerber et al., 2011; Zolotov, 2011; Zolotov et al., 2013). Oldhamite (CaS) and niningerite (MgS) have been suggested as major sulfide species on Mercury's surface (Nittler et al., 2011). This is in agreement with our predictions as shown in Figure 9.

Finally, the availability of SO_2 in a natural volcanic gas is not only controlled by the bulk abundance of S in the gas, but also by the oxygen fugacity of the gas. With increasingly reducing conditions SO_2 may be reduced to SO, S_2O, and S_2. In reduced C-bearing gases, such as predicted for the Moon and Mercury, reduced S-gases may include CS_2, COS, and CS (Renggli et al., 2017; Zolotov, 2011). In water-rich volcanic gas such as on Earth, the dominant reduced S-bearing gas species is H_2S (Henley & Seward, 2018). These reduced S-gas species have different molecular properties and their behavior during chemisorption reactions differs from SO_2 (King et al., 2018). This difference may particularly affect the kinetics of the gas-solid reaction, whereas the reaction may still result in the formation of sulfides as predicted in Figure 9. Our experiments using pure SO_2 do not allow predictions on the kinetics of reactions with other S-gas species as they occur in natural volcanic

gases. Specifically, future work will require experiments exploring gas-solid reactions with S at reducing conditions applicable to the Moon or Mercury.

4.4. Conclusions

Our experiments reveal that reactions between SO_2 and basaltic glasses produce $CaSO_4$, $MgSO_4$, Na_2SO_4, Fe-, Fe-Ti-(Al)-, and Ti- oxides, and silica coatings with pyroxenes and Fe-Ti-oxide crystallites in the glass substrates. This is in contrast to previous experimental studies, which observed a prevalence of $CaSO_4$ as the sole or dominant reaction product in reactions between SO_2 and silicate glasses (Ayris et al., 2013; Renggli et al., 2019). The experiments reveal a complex gas-solid reaction mechanism, whereby mobile elements such as Ca, Mg, Na, and Fe are lost to surface coatings rich in sulfate and oxide minerals, and silicate phases nucleate close to the surface of the glass. Our characterization of the products of SO_2-basalt experiments may be applied to understanding the mineralogy and chemistry of planetary settings where high-temperature gas-solid reactions occur, such as volcanic environments where SO_2-bearing gas and basalts are observed to coexist.

Acknowledgments
This research was supported by the Australian Research Council funding to King (DP150104604 and FT130101524). Renggli was supported by an ANU PhD scholarship. Palm was supported by the John and Kerry Lovering Scholarship (RSES, ANU). The Ion Probe Facility at the University of Western Australia is supported by the Australian Microscopy and Microanalysis Research Facility, AuScope, the Science and Industry Endowment Fund, and the State Government of Western Australia. The authors acknowledge the facilities and technical assistance of the Australian Microscopy and Microanalysis Research Facility at the Centre of Advanced Microscopy at the ANU, and the ANU Raman Facility in the Research School of Physics and Engineering. We acknowledge three anonymous reviewers for helpful comments on an earlier version of this paper in Renggli's PhD thesis. We thank Dick Henley for conversations that contributed to the work. The data used in this paper are available at Mendeley Data (https://doi.org/10.17632/hxh7j5g996.2). We thank Hanna Nekvasil and an anonymous reviewer for their helpful comments.

References

Angeli, F., Delaye, J.-M., Charpentier, T., Petit, J.-C., Ghaleb, D., & Faucon, P. (2000). Influence of glass chemical composition on the Na–O bond distance: A ^{23}Na 3Q-MAS NMR and molecular dynamics study. *Journal of Non-Crystalline Solids*, *276*(1-3), 132–144. https://doi.org/10.1016/S0022-3093(00)00259-3

Ayris, P. M., Lee, A. F., Wilson, K., Kueppers, U., Dingwell, D. B., & Delmelle, P. (2013). SO_2 sequestration in large volcanic eruptions: High-temperature scavenging by tephra. *Geochimica et Cosmochimica Acta*, *110*, 58–69. https://doi.org/10.1016/j.gca.2013.02.018

Ballhaus, C. (1993). Redox states of lithospheric and asthenospheric upper mantle. *Contributions to Mineralogy and Petrology*, *114*(3), 331–348. https://doi.org/10.1007/BF01046536

Barone, G., Mazzoleni, P., Corsaro, R. A., Costagliola, P., Di Benedetto, F., Ciliberto, E., et al. (2016). Nanoscale surface modification of Mt. Etna volcanic ashes. *Geochimica et Cosmochimica Acta*, *174*, 70–84. https://doi.org/10.1016/j.gca.2015.11.011

Basaltic Volcanism Study Project (1981). *Basaltic volcanism on the terrestrial planets* (p. 1286). Pergamon, New York: Pergamon Press.

Berger, G., Cathala, A., Fabre, S., Borisova, A., Pages, A., Aigouy, T., et al. (2019). An experimental exploration of volcanic rocks-atmosphere interaction under Venus surface conditions. *Icarus*, *329*, 8–23. https://doi.org/10.1016/j.icarus.2019.03.033

Blaney, D. L., Johnson, T. V., Matson, D. L., & Veeder, G. J. (1995). Volcanic eruptions on Io: Heat flow, resurfacing, and lava composition. *Icarus*, *113*(1), 220–225. https://doi.org/10.1006/icar.1995.1020

Burkhard, D. J. M. (2001). Crystallization and oxidation of Kilauea basalt glass: Processes during reheating experiments. *Journal of Petrology*, *42*(3), 507–527. https://doi.org/10.1093/petrology/42.3.507

Burnham, C. W. (1979). Magmas and hydrothermal fluids. In H. L. Barnes (Ed.), *Geochemistry of hydrothermal ore deposits* (pp. 71–136).

Buzgar, N., Buzatu, A., & Sanislav, I. V. (2009). The Raman study on certain sulfates. *Geologie*, *55*, 5–23.

Carmichael, I. S. (1991). The redox states of basic and silicic magmas: A reflection of their source regions? *Contributions to Mineralogy and Petrology*, *106*(2), 129–141. https://doi.org/10.1007/BF00306429

Carn, S. A., Clarisse, L., & Prata, A. J. (2016). Multi-decadal satellite measurements of global volcanic degassing. *Journal of Volcanology and Geothermal Research*, *311*, 99–134. https://doi.org/10.1016/j.jvolgeores.2016.01.002

Carr, M. H. (1986). Silicate volcanism on Io. *Journal of Geophysical Research*, *91*, 3521–3532.

Casas, A. S., Wadworth, F. B., Ayris, P. M., Delmelle, P., Vasseur, J., Cimarelli, C., & Dingwell, D. B. (2019). SO_2 scrubbing during percolation through rhyolitic volcanic domes. *Geochimica et Cosmochimica Acta*, *257*, 150–162. https://doi.org/10.1016/j.gca.2019.04.013

Castle, N., & Herd, C. D. K. (2017). Experimental petrology of the Tissint meteorite: Redox estimates, crystallization curves, and evaluation of petrogenetic models. *Meteoritics and Planetary Science*, *52*(1), 125–146. https://doi.org/10.1111/maps.12739

Cook, G. B., & Cooper, R. F. (2000). Iron concentration and the physical processes of dynamic oxidation in an alkaline earth aluminosilicate glass. *American Mineralogist*, *85*(3-4), 397–406. https://doi.org/10.2138/am-2000-0401

Cook, G. B., Cooper, R. F., & Wu, T. (1990). Chemical diffusion and crystalline nucleation during oxidation of ferrous iron-bearing magnesium aluminosilicate glass. *Journal of Non-Crystalline Solids*, *120*(1-3), 207–222. https://doi.org/10.1016/0022-3093(90)90205-Z

Cooper, R. F. (2020). Redox thermodynamics and kinetics in silicate melts and glasses—and related morphology/texture. In P. Richet (Ed.), *Encyclopedia of glass science, technology, history and culture*. New York: Wiley/American Ceramic Society, ISBN 978-1-118-79942-0 (https://www.wiley.com/en-us/Encyclopedia+of+Glass+Science%2C+Technology%2C+History%2C+and+Culture-p-9781118799420)

Cooper, R. F., Fanselow, J. B., & Poker, D. B. (1996). The mechanism of oxidation of a basaltic glass: Chemical diffusion of network-modifying cations. *Geochimica et Cosmochimica Acta*, *60*(17), 3253–3265. https://doi.org/10.1016/0016-7037(96)00160-3

Dalby, K. N., Berger, J. A., Brand, H. E. A., Cairney, J. M., Eder, K., Eggins, S. M., et al. (2018). Analytical techniques for probing gases and small-scale layers that preserve information on gas-solid interactions. *Reviews in Mineralogy and Geochemistry*, *84*(1), 103–175. https://doi.org/10.2138/rmg.2018.84.4

Day, J. M. D., Moynier, F., & Shearer, C. K. (2017). Late-stage magmatic outgassing from a volatile-depleted Moon. *Proceedings of the National Academy of Sciences of the United States of America*, *114*, 9457–9551.

Delmelle, P., Wadsworth, F. B., Maters, E. C., & Ayris, P. M. (2018). High temperature uptake of volcanic gases on ash in eruption plumes. *Reviews in Mineralogy and Geochemistry*, *84*(1), 285–308. https://doi.org/10.2138/rmg.2018.84.8

Denevi, B. W., Ernst, C. M., Meyer, H. M., Robinson, M. S., Murchie, S. L., Whitten, J. L., et al. (2013). The distribution and origin of smooth plains on Mercury. *Journal of Geophysical Research: Planets*, *118*, 891–907. https://doi.org/10.1002/jgre.20075

Doute, S. (2002). Dynamics and evolution of SO_2 gas condensation around Prometheus-like volcanic plumes on Io as seen by the near infrared mapping spectrometer. *Icarus*, *158*(2), 460–482. https://doi.org/10.1006/icar.2002.6889

Dufresne, C. D. M., King, P. L., Dyar, M. D., & Dalby, K. N. (2015). Effect of SiO_2, total FeO, Fe^{3+}/Fe^{2+}, and alkali elements in basaltic glasses on mid-infrared spectra. *American Mineralogist*, *94*, 1580–1590.

Evans, H. T. (1979). The thermal expansion of anhydrite to 1000 °C. *Physics and Chemistry of Minerals*, *4*(1), 77–82. https://doi.org/10.1007/BF00308361

Fegley, B., & Prinn, R. G. (1989). Estimation of the rate of volcanism on Venus from reaction rate measurements. *Nature*, *337*(6202), 55–58. https://doi.org/10.1038/337055a0

Fegley, B., Zolotov, M. Y., & Lodders, K. (1997). The oxidation state of the lower atmosphere and surface of Venus. *Icarus*, *125*(2), 416–439. https://doi.org/10.1006/icar.1996.5628

Franz, H. B., King, P. L., & Gaillard, F. (2018). Sulfur on Mars from the atmosphere to the core. In J. Filiberto, & S. P. Schwenzer (Eds.), *Volatiles in the Martian crust* (pp. 119–183). Elsevier.

Gaillard, F., Michalski, J., Berger, G., McLennan, S., & Scaillet, B. (2013). Geochemical reservoirs and timing of sulfur cycling on Mars. *Space Science Reviews*, *174*(1-4), 251–300. https://doi.org/10.1007/s11214-012-9947-4

Gaillard, F., & Scaillet, B. (2009). The sulfur content of volcanic gases on Mars. *Earth and Planetary Science Letters*, *279*(1-2), 34–43. https://doi.org/10.1016/j.epsl.2008.12.028

Gerlach, T. M. (1980). Evaluation of volcanic gas analysis from Kilauea volcano. *Journal of Volcanology and Geothermal Research*, *7*(3-4), 295–317. https://doi.org/10.1016/0377-0273(80)90034-7

Gislason, S. R., Hassenkam, T., Nedel, S., Bovet, N., Eiriksdottir, E. S., Alfredsson, H. A., et al. (2011). Characterization of Eyjafjallajökull volcanic ash particles and a protocol for rapid risk assessment. *Proceedings of the National Academy of Sciences*, *108*(18), 7307–7312. https://doi.org/10.1073/pnas.1015053108

Glaze, L. S. (1999). Transport of SO_2 by explosive volcanism on Venus. *Journal of Geophysical Research*, *104*(E8), 18,899–18,906. https://doi.org/10.1029/1998JE000619

Graves, P. R., Johnston, C., & Campaniello, J. J. (1988). Raman scattering in spinel structure ferrites. *Materials Research Bulletin*, *23*(11), 1651–1660. https://doi.org/10.1016/0025-5408(88)90255-3

Hapanowicz, R. P., & Condrate, S. R. A. (1996). Raman spectral investigation of sulfate inclusions in sodium calcium silicate glasses. *Journal of Solid State Chemistry*, *123*(1), 183–185. https://doi.org/10.1006/jssc.1996.0166

Haskin, L., & Warren, P. (1991). Lunar chemistry. In G. H. Heiken, D. T. Vaniman, & B. M. French (Eds.), *Lunar Sourcebook* (pp. 357–474). Cambridge University Press.

Henley, R. W., Brink, F. J., King, P. L., Leys, C., Ganguly, J., Mernagh, T., et al. (2017). High temperature gas–solid reactions in calc–silicate Cu–Au skarn formation; Ertsberg, Papua Province, Indonesia. *Contributions to Mineralogy and Petrology*, *172*(11-12), 106–124. https://doi.org/10.1007/s00410-017-1413-6

Henley, R. W., King, P. L., Wykes, J. L., Renggli, C. J., Brink, F. J., Clark, D. A., & Troitzsch, U. (2015). Porphyry copper deposit formation by sub-volcanic sulphur dioxide flux and chemisorption. *Nature Geoscience*, *8*(3), 210–215. https://doi.org/10.1038/ngeo2367

Henley, R. W., & Seward, T. M. (2018). Gas-solid reactions and reactive mass transport in volcanic systems. *Reviews in Mineralogy and Geochemistry*, *84*(1), 309–349. https://doi.org/10.2138/rmg.2018.84.9

Hirschmann, M. M., & Withers, A. C. (2008). Ventilation of CO_2 from a reduced mantle and consequences for the early Martian greenhouse. *Earth and Planetary Science Letters*, *270*(1-2), 147–155. https://doi.org/10.1016/j.epsl.2008.03.034

Holloway, J. R., & Burnham, C. W. (1972). Melting relations of basalt with equilibrium water pressure less than total pressure. *Journal of Petrology*, *13*(1), 1–29. https://doi.org/10.1093/petrology/13.1.1

Ilyinskaya, E., Schmidt, A., Mather, T. A., Pope, F. D., Witham, C., Baxter, P., et al. (2017). Understanding the environmental impacts of large fissure eruptions: Aerosol and gas emissions from the 2014-2015 Holuhraun eruption (Iceland). *Earth and Planetary Science Letters*, *472*, 309–322. https://doi.org/10.1016/j.epsl.2017.05.025

Kerber, L., Head, J. W., Blewett, D. T., Solomon, S. C., Wilson, L., Murchie, S. L., et al. (2011). The global distribution of pyroclastic deposits on Mercury: The view from MESSENGER flybys 1–3. *Planetary and Space Science*, *59*(15), 1895–1909. https://doi.org/10.1016/j.pss.2011.03.020

Kerber, L., Head, J. W., Solomon, S. C., Murchie, S. L., Blewett, D. T., & Wilson, L. (2009). Explosive volcanic eruptions on Mercury: Eruption conditions, magma volatile content, and implications for interior volatile abundances. *Earth and Planetary Science Letters*, *285*(3-4), 263–271. https://doi.org/10.1016/j.epsl.2009.04.037

King, P. L., Hervig, R. L., Holloway, J. R., Delaney, J. S., & Dyar, M. D. (2000). Partitioning of Fe^{3+}/Fe_{total} between amphibole and basanitic melt as a function of oxygen fugacity. *Earth and Planetary Science Letters*, *178*(1-2), 97–112. https://doi.org/10.1016/S0012-821X(00)00071-6

King, P. L., & McLennan, S. M. (2010). Sulfur on Mars. *Elements*, *6*(2), 107–112. https://doi.org/10.2113/gselements.6.2.107

King, P. L., & McSween, H. Y. Jr. (2005). Effects of H_2O, pH and oxidation state on the stability of Fe-minerals on Mars. *Journal of Geophysical Research*, *110*, E12S10. https://doi.org/10.1029/2005JE002482

King, P. L., Wheeler, V. W., Renggli, C. J., Palm, A. B., Wilson, S. A., Harrison, A. L., et al. (2018). Experimental approaches and theoretical aspects of gas-solid reactions with case studies. *Reviews in Mineralogy and Geochemistry*, *84*(1), 1–56. https://doi.org/10.2138/rmg.2018.84.1

Kress, V. C., & Carmichael, I. S. (1991). The compressibility of silicate liquids containing Fe_2O_3 and the effect of composition, temperature, oxygen fugacity and pressure on their redox states. *Contributions to Mineralogy and Petrology*, *108*(1-2), 82–92. https://doi.org/10.1007/BF00307328

Kumar, S. (1985). The SO_2 atmosphere and ionosphere of Io: Ion chemistry, atmospheric escape, and models corresponding to the Pioneer 10 radio occultation measurements. *Icarus*, *61*(1), 101–123. https://doi.org/10.1016/0019-1035(85)90158-7

Le Losq, C., & Neuville, D. R. (2017). Molecular structure, configurational entropy and viscosity of silicate melts: Link through the Adam and Gibbs theory of viscous flow. *Journal of Non-Crystalline Solids*, *463*, 175–188. https://doi.org/10.1016/j.jnoncrysol.2017.02.010

Le Losq, C., Neuville, D. R., Florian, P., Henderson, G. S., & Massiot, D. (2014). The role of Al^{3+} on rheology and structural changes in sodium silicate and aluminosilicate glasses and melts. *Geochimica et Cosmochimica Acta*, *126*, 495–517. https://doi.org/10.1016/j.gca.2013.11.010

Liu, Y., Wang, A., & Freemen, J. J. (2009). Raman, MIR, and NIR spectroscopic study of calcium sulfates: Gypsum, bassanite, and anhydrite. *Lunar and Planetary Science Conference*, *40*, 2128.

Lopez-Reyes, G., Sobron, P., Lefebvre, C., & Rull, F. (2014). Multivariate analysis of Raman spectra for the identification of sulfates: Implications for ExoMars. *American Mineralogist*, *99*(8-9), 1570–1579. https://doi.org/10.2138/am.2014.4724

McCanta, M. C., Dyar, M. D., & Treiman, A. H. (2014). Alteration of Hawaiian basalts under sulfur-rich conditions: Applications to understanding surface-atmosphere interactions on Mars and Venus. *American Mineralogist*, *99*(2-3), 291–302. https://doi.org/10.2138/am.2014.4584

McCollom, T., Robbins, M., Moskowitz, B., Berquo, T. S., Jöns, N., & Hynek, B. M. (2013). Experimental study of acid-sulfate alteration of basalt and implications for sulfate deposits on Mars: Acid-sulfate alteration of basalt. *Journal of Geophysical Research: Planets*, *118*, 577–614. https://doi.org/10.1002/jgre.20044

McCubbin, F. M., Riner, M. A., Vander Kaaden, K. E., & Burkemper, L. K. (2012). Is Mercury a volatile-rich planet? *Geophysical Research Letters*, *39*, L09202. https://doi.org/10.1029/2012gl051711

McSween, H. Y., Ruff, S. W., Morris, R. V., Bell, J. F., Herkenhoff, K., Gellert, R., et al. (2006). Alkaline volcanic rocks from the Columbia Hills, Gusev crater, Mars. *Journal of Geophysical Research*, *111*, E09S91. https://doi.org/10.1029/2006je002698

Mernagh, T. P., King, P. L., McMillan, P. F., Berger, J. A., & Dalby, K. N. (2018). Using infrared and Raman spectroscopy to analyze gas-solid reactions. *Reviews in Mineralogy and Geochemistry*, *84*(1), 177–228. https://doi.org/10.2138/rmg.2018.84.5

Morris, R. V., Agresti, D. G., Lauer, H. V., Newcomb, J. A., Shelfer, T. D., & Murali, A. V. (1989). Evidence for pigmentary hematite on Mars based on optical, magnetic, and Mössbauer studies of superparamagnetic (nanocrystalline) hematite. *Journal of Geophysical Research*, *94*(B3), 2760–2778. https://doi.org/10.1029/JB094iB03p02760

Mysen, B. O., & Richet, P. (2005). *Silicate glasses and melts: Properties and structure*. Boston: Elsevier, Amsterdam.

Neuville, D. R., & Mysen, B. O. (1996). Role of aluminium in the silicate network: In situ, high-temperature study of glasses and melts on the join SiO_2-$NaAlO_2$. *Geochimica et Cosmochimica Acta*, *60*(10), 1727–1737. https://doi.org/10.1016/0016-7037(96)00049-X

Nimmo, F., & McKenzie, D. (1998). Volcanism and tectonics on Venus. *Annual Review of Earth and Planetary Sciences*, *26*(1), 23–51. https://doi.org/10.1146/annurev.earth.26.1.23

Nittler, L. R., Starr, R. D., Weider, S. Z., McCoy, T. J., Boynton, W. V., Ebel, D. S., et al. (2011). The major-element composition of Mercury's surface from MESSENGER X-ray spectrometry. *Science*, *333*(6051), 1847–1850. https://doi.org/10.1126/science.1211567

O'Neill, H. S. C., & Pownceby, M. I. (1993). Thermodynamic data from redox reactions at high temperatures. I. An experimental and theoretical assessment of the electrochemical method using stabilized zirconia electrolytes, with revised values for the Fe-"FeO", Co-CoO, Ni-NiO and Cu-Cu_2O oxygen buffers, and new data for the W-WO_2 buffer. *Contributions to Mineralogy and Petrology*, *114*, 296–314.

Oppenheimer, C., Moretti, R., Kyle, P. R., Eschenbacher, A., Lowenstern, J. B., Hervig, R. L., & Dunbar, N. W. (2011). Mantle to surface degassing of alkalic magmas at Erebus volcano, Antarctica. *Earth and Planetary Science Letters*, *306*(3-4), 261–271. https://doi.org/10.1016/j.epsl.2011.04.005

Palm, A. B., King, P. L., Renggli, C. J., Hervig, R. L., Dalby, K. N., Herring, A., et al. (2018). Unravelling the consequences of SO_2-basalt reactions for geochemical fractionation and mineral formation. *Reviews in Mineralogy and Geochemistry*, *84*(1), 257–283. https://doi.org/10.2138/rmg.2018.84.7

Pearl, J., Hanel, R., Kunde, V., Maguire, W., Fox, K., Gupta, S., et al. (1979). Identification of gaseous SO_2 and new upper limits for other gases on Io. *Nature*, *280*(5725), 755–758. https://doi.org/10.1038/280755a0

Renggli, C. J., & King, P. L. (2018). SO_2 gas reactions with silicate glasses. *Reviews in Mineralogy and Geochemistry*, *84*(1), 229–255. https://doi.org/10.2138/rmg.2018.84.6

Renggli, C. J., King, P. L., Henley, R. W., Guagliardo, P., McMorrow, L., Middleton, J., & Turner, M. (2019). An experimental study of SO_2 reactions with silicate glasses and supercooled melts in the system anorthite-diopside-albite at high temperature. *Contributions to Mineralogy and Petrology*, *174*(1), 3–21. https://doi.org/10.1007/s00410-018-1538-2

Renggli, C. J., King, P. L., Henley, R. W., & Norman, M. D. (2017). Volcanic gas composition, metal dispersion and deposition during explosive volcanic eruptions on the Moon. *Geochimica et Cosmochimica Acta*, *206*, 296–311. https://doi.org/10.1016/j.gca.2017.03.012

Roine, A. (2015). Outotec HSC Chemistry 8.1. Outotec Research Center, Finland.

Rose, W. I. (1977). Scavenging of volcanic aerosol by ash: Atmospheric and volcanologic implications. *Geology*, *5*(10), 621–624. https://doi.org/10.1130/0091-7613(1977)5<621:SOVABA>2.0.CO;2

Rutherford, M. J., & Papale, P. (2009). Origin of basalt fire-fountain eruptions on Earth versus the Moon. *Geology*, *37*(3), 219–222. https://doi.org/10.1130/G25402A.1

Ryan, M. P., & Sammis, C. G. (1981). The glass transition in basalt. *Journal of Geophysical Research*, *86*(B10), 9519–9535. https://doi.org/10.1029/JB086iB10p09519

Schiffman, P., Zierenberg, R., Marks, N., Bishop, J. L., & Dyar, M. D. (2006). Acid-fog deposition at Kilauea volcano: A possible mechanism for the formation of siliceous-sulfate rock coatings on Mars. *Geology*, *31*, 921–924.

Shearer, C. K., Sharp, Z. D., Burber, P. V., McCubbin, F. M., Provencio, P. P., Brearley, A. J., & Steele, A. (2014). Chlorine distribution and its isotopic composition in "rusty rock" and lunar soils, origin of "rusty" alteration, and volatile element behavior on the Moon. *Geochimica et Cosmochimica Acta*, *139*, 411–433. https://doi.org/10.1016/j.gca.2014.04.029

Starr, R. D., Schriver, D., Nittler, L. R., Wieder, S., Byrne, P. K., Ho, G. C., et al. (2012). MESSENGER detection of electron-induced X-ray fluorescence from Mercury's surface. *Journal of Geophysical Research*, *117*, E00L02. https://doi.org/10.1029/2012je004118

Taylor, S. R., & McLennan, S. (2009). *Planetary crusts: Their composition, origin and evolution* (p. 278). Cambridge, UK: Cambridge University Press.

Tompsett, G. A., Bowmaker, G. A., Cooney, R. P., Metson, J. B., Rodgers, K. A., & Seakins, J. M. (1995). The Raman spectrum of brookite, TiO_2 (Pbca, Z = 8). *Journal of Raman Specroscopy*, *26*(1), 57–62. https://doi.org/10.1002/jrs.1250260110

Tröger, W. E. (2017). In H. U. Bambauer, F. Taborszky, & H. Dieter (Eds.), *Optische Bestimmung der gesteinsbildenden Minerale Teil I.: Bestimmungstabellen* (p. 188). Stuttgart, Germany: Schweizerbart Science Publishers.

Vandaele, A. C., Korablev, O., Belyaev, D., Chamberlain, S., Evdokimova, D., Encrenaz, T., et al. (2017). Sulfur dioxide in the Venus Atmosphere: II. Spatial and temporal variability. *Icarus*, *295*, 1–15.

Wang, A., Freeman, J. J., Jolliff, B. L., & Chou, I.-M. (2006). Sulfates on Mars: A systematic Raman spectroscopic study of hydration states of magnesium sulfates. *Geochimica et Cosmochimica Acta*, *70*(24), 6118–6135. https://doi.org/10.1016/j.gca.2006.05.022

Weider, S. Z., Nittler, L. R., Starr, R. D., McCoy, T. J., Stockstill-Cahill, K. R., Byrne, P. K., et al. (2012). Chemical heterogeneity on Mercury's surface revealed by MESSENGER X-ray spectrometer: Chemical heterogeneity on Mercury. *Journal of Geophysical Research*, *117*, E00L05. https://doi.org/10.1029/2012je004153

Zolotov, M. Y. (2011). On the chemistry of mantle and magmatic volatiles on Mercury. *Icarus*, *212*(1), 24–41. https://doi.org/10.1016/j.icarus.2010.12.014

Zolotov, M. Y. (2018). Gas-solid interactions on Venus and other solar system bodies. *Reviews in Mineralogy and Geochemistry*, *84*(1), 351–392. https://doi.org/10.2138/rmg.2018.84.10

Zolotov, M. Y., & Fegley, B. (1999). Oxidation state of volcanic gases and the interior of Io. *Icarus*, *141*(1), 40–52. https://doi.org/10.1006/icar.1999.6164

Zolotov, M. Y., & Fegley, B. (2000). Eruption conditions of Pele volcano on Io inferred from chemistry of its volcanic plume. *Geophysical Research Letters*, *27*(17), 2789–2792. https://doi.org/10.1029/2000GL011608

Zolotov, M. Y., Sprague, A. L., Hauck, S. A., Nittler, L. R., Solomon, S. C., & Wieder, S. Z. (2013). The redox state, FeO content, and origin of sulfur-rich magmas on Mercury. *Geophysical Research Letters*, *118*, 138–146. https://doi.org/10.1029/2012JE004274

Zoppi, A., Lofrumento, C., Castellucci, E. M., & Sciau, P. (2008). Al-for-Fe substitution in hematite: the effect of low Al concentrations in the Raman spectrum of Fe_2O_3. *Journal of Raman Specroscopy*, *39*(1), 40–46. https://doi.org/10.1002/jrs.1811